# Effects of non-retinal inputs in visual thalamus depend on visual responsiveness and stimulus context

**Lisa Schmors[1,2,*], Ann H. Kotkat[3,4,*], Yannik Bauer[3,4,*], Ziwei Huang[1,2], Davide Crombie[3,4], Lukas Meyerolbersleben[3,4], Sacha Sokoloski[1,2], Philipp Berens[1,2,+], and Laura Busse[3,5,+]**

[1]Hertie Institute for AI in Brain Health, University of Tübingen, 72076 Tübingen, Germany
[2]Tübingen AI Center, University of Tübingen, 72076 Tübingen, Germany
[3]Division of Neuroscience, Faculty of Biology, LMU Munich, 82152 Munich, Germany
[4]Graduate School of Systemic Neurosciences (GSN), LMU Munich, 82152 Munich, Germany
[5]Bernstein Center for Computational Neuroscience, 82152 Munich, Germany
[*]These authors contributed equally to this work
[+]Correspondence: busse@bio.lmu.de (L.B.), philipp.berens@uni-tuebingen.de (P.B.)

## ABSTRACT

In the dorsolateral geniculate nucleus (dLGN) of the thalamus, retinal signals are combined with non-retinal inputs such as corticothalamic (CT) feedback and behavioural state. How these shape dLGN activity remains an open question. We recorded extracellular responses in dLGN of awake mice to a movie stimulus, while photosuppressing CT feedback, tracking locomotion and pupil size. To assess the relative impact of retinal and non-retinal inputs, we fit single neuron responses using generalized linear models. While including CT feedback and behavioural state as predictors significantly improved the model's overall performance, the improvement was especially pronounced for a sub-population of poorly visually responsive neurons. In addition, the impact of CT feedback was faster and more prevalent in the absence of a patterned visual stimulus. Finally, for CT feedback-sensitive dLGN neurons, visual stimuli could be discriminated better when CT feedback was suppressed. Together, these results show that effects of non-retinal inputs in dLGN depend on visual responsiveness and stimulus context.

## Introduction

Visual information is processed in a hierarchy of brain areas, which are connected through feedforward and feedback projections. Towards the beginning of this hierarchy is the dorsolateral geniculate nucleus (dLGN) of the thalamus, a central node for visual information on the path from the retina to the primary visual cortex (V1) (*1, 2*). It is one of the first visual stages that combines inputs from multiple visual and non-visual sources (*3*). This combination of inputs transforms the feedforward responses (*4, 5, 6, 7*), sharpens spatial and temporal receptive field (RF) properties (*8*), provides contextual modulations by L6 cortico-thalamic (CT) feedback (*9, 10, 11, 12, 13*), and modulates responses according to the animal's behavioural state (*14, 3, 15, 16, 17*). While these factors have often been studied in isolation, it is still poorly understood how feedforward retinal input and the modulations by CT feedback and behavioural state act in combination to shape dLGN responses, in particular during wakefulness and in the context of a rich naturalistic visual stimulus.

Past studies have investigated how CT feedback and behavioural state act separately on dLGN activity. On the one hand, the modulatory effects of CT feedback have been shown to be diverse (*18, 19*), such that there is little consensus on its overall functional role: While CT feedback can sharpen spatial and temporal properties of dLGN RFs (*20, 21, 22, 11, 23*), its effects on overall firing rate seems mixed and potentially stimulus-dependent. On the other hand, the dLGN has long been known as one of the earliest stages in the visual hierarchy in which activity is shaped by the animal's behavioural state (*24, 25, 26*). For instance, in the mouse, locomotion- (*27, 28*) or pupil-indexed arousal (*15, 16, 17, 29*) can lead to dLGN response enhancements. Overall, however, we lack a quantitative understanding of the relative strengths of these non-retinal effects on dLGN responses during wakefulness and how they might interact and depend on retinal input.

Generalized linear models (GLMs) provide an established framework for statistical analysis of neural responses, that can help us disentangle the combined impact of multiple visual and non-visual influences and investigate their properties (*30, 31, 32, 33*). While GLMs are relatively simple phenomenological models, they offer the advantage of being interpretable: for instance, GLM kernels learned for the visual stimulus approximate the integration by the spatio-temporal RF, and kernels learned for any additional inputs represent spike-induced gain adjustments (*34, 31*). First applied in the retina (*35, 31*), GLMs have

since then been used in numerous studies to separate influences of the visual stimulus and other variables, like spike history, interneuronal interaction effects, task-engagement, learning, reward prediction, task-related motor action, locomotion, and arousal (*36, 37, 38, 39, 40, 41, 42*). One recent extension of classical GLMs is to estimate RFs by choosing a set of cubic spline basis functions in order to encode smoothness, decrease the number of parameters, and thus be more data efficient (*43*).

Here, we investigated how feedforward signals, feedback signals, and behavioural state jointly influence dLGN activity in awake, head-fixed mice viewing a rich movie stimulus. We simultaneously recorded extracellular dLGN activity, mouse run speed and pupil size, while photosuppressing CT feedback. We then fitted a spline-GLM model containing predictors for the spatio-temporal RF, CT feedback and behaviour to predict responses of dLGN neurons. The learned kernels were biologically plausible, including diverse spatio-temporal RFs aligned with their functional type, as well as kernels for CT feedback and behaviour. While including these non-retinal predictors improved the prediction of dLGN responses overall, improvements were most prominent for a subpopulation of poorly visually responsive neurons. Furthermore, comparing the learned CT feedback kernels for stimulation with movies and gray screen revealed that effects of CT feedback were stronger, more prevalent and faster during the absence of a patterned visual stimulus. Finally, we used the spline-GLM for *in silico* experiments isolating the impact of CT feedback suppression, and demonstrate that stimulus discrimination for CT feedback-responsive neurons was enhanced. We conclude that effects of non-retinal inputs in dLGN depend on visual responsiveness and stimulus context.

## Results

### dLGN responses to movies are modulated by behavioural variables and L6CT feedback suppression

To investigate how CT feedback, locomotion and arousal modulate thalamic responses, we recorded *in vivo* extracellular dLGN activity in response to a rich movie stimulus in head-fixed mice together with running speed and pupil size, while randomly photo-suppressing L6CT feedback (**Figure 1a**). For photo-suppression of L6CT feedback, we conditionally expressed the soma-targeting, chloride-conducting channelrhodopsin stGtACR2-RFP (*44*) in L6CT pyramidal cells, by injecting a small volume of Cre-dependent AAV into V1 of Ntsr1-Cre mice (*45*). The localisation of stGtACR2 to L6CT somata and the accurate placement of electrodes were confirmed through post-mortem histological analyses (**Figure 1b**). During the recordings, photo-suppression occurred with 50% probability in each second. At the same time, the mouse viewed a rich movie stimulus that consisted of a sequence of black-and-white clips from various feature films ('movies', **Figure 1c**).

During the presentation of the movie stimulus, we observed a wide range of dLGN responses. As illustrated for a short segment of an example recording session (**Figure 1c**), the simultaneously recorded dLGN neurons showed different overall firing rates and modulation by behaviour. This likely reflected differential sensitivity to the various inputs, including the time-varying features of the movie stimulus, the random periods of photo-suppression of CT feedback, and fluctuations in the behavioural state of the animal, which we inferred from the animal's running speed and pupil size (*27, 28, 15, 7*). For instance, periods of larger run speed and larger pupil seemed to coincide with a general increase in firing rates.

To develop our initial insights into the modulations of dLGN responses by CT feedback and the other potentially modulating inputs, we aligned movie responses to photo-suppression, running onsets, and pupil dilation. We found that certain neurons responded to CT feedback suppression with a substantial reduction in firing rate (**Figure 1d,e**), while others showed milder effects or no modulation at all (**Figure 1f**). Consistent with previous findings we also found that during our movie stimulus, firing rates could gradually increase around transitions from sitting to running (**Figure S1a**), and during pupil dilation (**Figure S1b**).

These modulations of responses by non-retinal factors were also observed across the population of recorded neurons. Specifically, dLGN firing rates during the time of V1 L6CT FB suppression compared to control windows were reduced (*control vs. CT FB supp.*: 12.6 vs. 11.5 Hz, $p = 1.24 \times 10^{-2}$, paired Wilcoxon signed-rank test; **Figure 1f, left**), while time windows with running and dilated pupil sizes were associated with an overall increase in average firing rates (*run vs. sit*: 12.8 vs. 11.0 Hz, $p = 8.31 \times 10^{-16}$, **Figure 1f, middle**; *large vs. small pupil*: 13.0 vs. 11.0 Hz, $p = 4.98 \times 10^{-7}$, paired Wilcoxon signed-rank test; **Figure 1f, right**). Although these modulations by non-retinal factors affected the recorded dLGN population on average, we also noticed considerable neuron-to-neuron variability. Indeed, for all three non-retinal inputs, we found that changes could span several orders of magnitude (**Figure 1f, insets**).

While so far, we showed that our movie stimulus elicited rich responses in dLGN, which were modulated by multiple non-retinal inputs, this simple analysis on the mean firing rates does not take into account potential correlations between the different inputs. Consistent with previous studies showing that pupil size and running indexing partially overlapping behavioural states (*46, 47, 16*), we found a positive correlation between pupil diameter and running speed ($r = 0.19 \pm 0.18$, mean $\pm$ SD; $p < 0.001$ for 5/6 experiments, permutation test; **Figure S1c**). Moreover, we found pupil size to also be influenced by stimulus brightness, where lower average intensity of movie frames was associated with larger pupil diameters ($r = -0.41 \pm 0.14$, mean $\pm$ SD; $p < 0.001$ for 6/6 experiments, permutation test; **Figure S1c**).

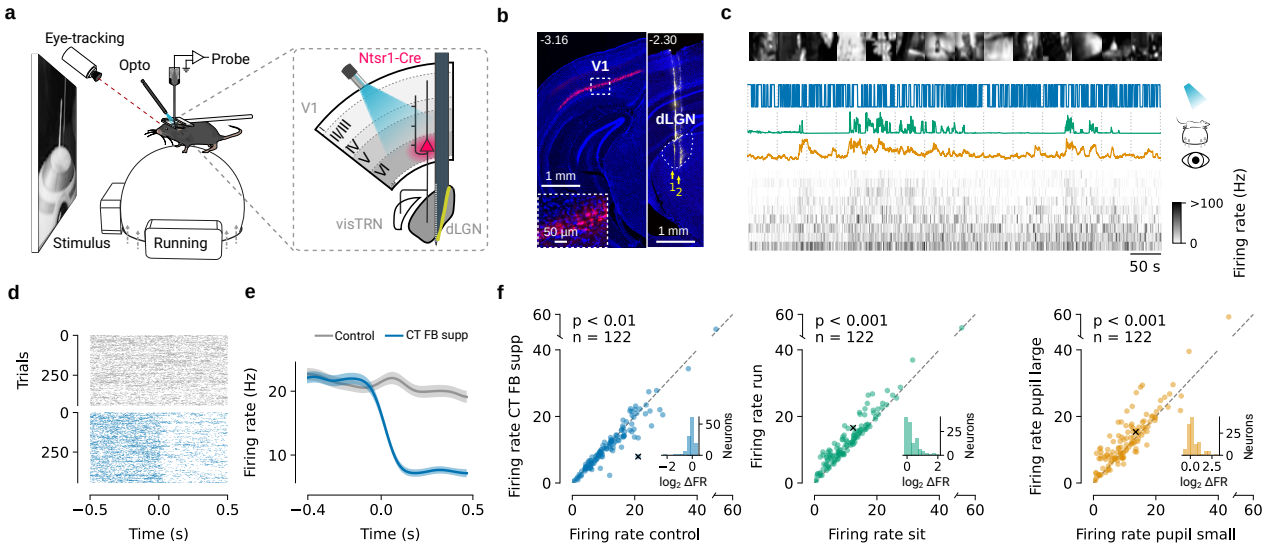


**Figure 1 | CT feedback and behaviour modulates dLGN responses to movies** (**a**) Schematic of the recording setup and photo-suppression of V1 L6CT pyramidal neurons in Ntsr1-Cre mice with Cre-dependent AAV-stGtACR2-RFP. (**b**) Histology. *Left:* Coronal section near V1 injection site, with stGtACR2-RFP expression (*red*) in Ntsr1+ somata. *Blue:* DAPI; scale bar: 1 mm. *Inset:* Magnification of area marked by dotted rectangle. Scale bar: 50 µm. *Right:* Coronal section of dLGN recording sites, with electrode tracks for two consecutive recording sessions (arrows 1 and 2) marked with DiI (*yellow*). Scale bar: 1 mm. *Dotted line*: dLGN contour. *Numbers on top*: position relative to Bregma in mm. (**c**) Snippet of an example dLGN recording. *Top to bottom*: example frames of the movie stimulus, photo-suppression pulse train (*blue*), running speed (*green*), pupil area (*yellow*), and time-varying firing rate (sorted by first principal component) of simultaneously recorded dLGN neurons. (**d**) Raster plot of responses of an example dLGN neuron, time locked to the onset of L6CT feedback photo-suppression (*blue*) and to control periods without photosuppression (*grey*). (**e**) Corresponding PSTHs. (**f**) Effects of L6CT FB photo-suppression (*left*), locomotion (*middle*), and pupil size (*right*) on dLGN mean firing rates. Example neuron from (d, e) marked with $\times$. $p$ values denote results of Wilcoxon signed-rank test, $n = 122$ neurons. *Insets:* Histogram of firing rate fold-change relative to control ($\Delta$ FR $\log_2$-ratio).

## A spline-based GLM captures dLGN spatio-temporal RFs and their modulation by L6CT feedback and behaviour

To disentangle how the various potential influences shape the responses of dLGN neurons, we used a generalized linear model (GLM) (*31*) that predicted the neuron's firing rate based on a combination of retinal (stimulus) and non-retinal inputs (running speed, pupil size, and CT feedback) (**Figure 2**). The model consisted of one linear kernel for each input, followed by a softplus function that accounted for response nonlinearities (**Figure 2a**). The shape of the stimulus kernel captured the neuron's spatio-temporal RF, while the shapes of the non-retinal kernels captured gain modulations of the neuron's firing (*31*). We employed a GLM with a spline basis in order to efficiently generate smooth kernels, rather than operating directly on the pixels of the visual stimulus or the discrete time bins of the additional inputs (*43*). The GLM also allowed us to effectively capture the temporal correlations between the inputs (see also above, **Figure S1c**), and the spatio-temporal correlations in pixel intensities in naturalistic stimuli (*48, 49*) (**Figure S2a**).

We trained and evaluated the spline-GLM on the recorded data set. Given the known diversity of mouse dLGN response properties (*50, 4*), we performed a separate hyperparameter search for each neuron. Hyperparameters included the number of spline bases for the retinal and non-retinal inputs and the weight for L1 regularization (see Methods). All GLM fits in this study were cross-validated. As standard procedure for time series data, we used 150 out of the 188 unique movie clips for cross-validation to select optimal hyperparameters and reserving the remaining 38 clips as a held-out test set (see Methods). The models analysed here were configured with the selected optimal hyperparameters and the reported performance is based on the held-out test set."

Following model fitting, we assessed the predictive power of the learned kernel shapes using a session-based permutation test (**Figure 2b**). To keep the temporal statistics of the time series data intact, we provided the model with input data recorded on a different day (for the model inputs 'stimulus', 'running', 'pupil size') or with synthetic inputs generated with the same statistics as the original (for the 'CT feedback suppression' input). Subsequently, we compared for each input the actual model performance (Pearson's $r$) against a distribution of model performances with that specific input permuted. Inputs were considered significant if the actual performance differed from the permuted performance with $p \leq 0.05$.

We observed a rich diversity of learned GLM kernels for the dLGN neurons' spatio-temporal RFs, the effects of CT feedback, and the behavioural variables. To begin with, we considered three example neurons (**Figure 2c**). Of these, the first had a negative spatial and a transient temporal stimulus response kernel, which contributed significantly to the model's performance (permutation test, $p = 3.51 \times 10^{-2}$; **Figure 2c$_1$, top**, same neuron as in **Figure 1d–e**). In addition, it had a significant negative kernel for CT FB suppression (permutation test, $p = 2.67 \times 10^{-4}$; **Figure 2c$_2$, c$_3$, top**). In contrast, the running and pupil size kernels had minimal impact on this neuron's model predictions (permutation test, $p > 0.05$). The second example neuron exhibited a positive spatial RF with an antagonistic surround (permutation test, $p = 2.31 \times 10^{-3}$; **Figure 2c$_1$, middle**). While both behavioural kernels seemed to contribute (**Figure 2c$_2$, middle**), only the kernel for pupil size reached significance in the permutation test ($p = 1.13 \times 10^{-2}$). This neuron was not influenced by CT FB suppression ($p > 0.05$; **Figure 2c$_2$, c$_3$, middle**). Finally, example neuron 3 was primarily visually driven, with a positive RF centre and a more sustained temporal response kernel (permutation test, $p = 2.31 \times 10^{-3}$; **Figure 2c$_1$, bottom**). It also had a significant negative kernel for CT FB suppression (permutation test, $p = 2.67 \times 10^{-4}$; **Figure 2c$_2$, c$_3$, bottom**). The other two non-retinal kernels had only negligible influences (permutation test, $p > 0.05$; **Figure 2c$_2$, c$_3$, bottom**).

The diversity observed in the three example neurons was also evident in the model fits across the population of recorded dLGN neurons, where we obtained a variety of spatio-temporal RFs, and combinations of non-retinal influences. Assessing the learned spatio-temporal kernels, we found that $\sim 70\%$ of the recorded dLGN neurons were visually responsive ($85/122$ neurons; permutation test visual stimulus, $p \leq 0.05$; **Figure S4a**). For these neurons (representative examples in **Figure 2d**), the spline-GLM recovered spatial RF properties that were consistent with previous descriptions of mouse dLGN RFs obtained using artificial stimuli (*50, 52, 53*). These properties included various RF locations, RFs with either positive (66%, 56/85 neurons) or negative polarity kernels (34%, 29/85 neurons), a broad range of RF surround strengths (**Figure S2b,d**), and various RF centre sizes (**Figure S2c**). Furthermore, the GLM captured the well-known diversity of temporal response properties of dLGN neurons (*54, 50*), with some neurons showing more sustained, and others showing more transient temporal kernels (**Figure 2e**). Importantly, both the spatial and temporal GLM kernels matched well with the polarity and the dynamics of the dLGN functional cell types. To assign functional cell types, we clustered step-responses to a full-field stimulus into Sustained-OFF, Sustained-ON, and Transient groups (see Methods, **Figure S3**). This correspondence further underscores our model's capacity to capture meaningful spatio-temporal RF properties and essential visual response characteristics of the recorded dLGN neurons.

We next assessed the learned kernels for the non-retinal inputs, and found significant modulatory effects. According to the permutation test, approximately 10% (12/122 neurons) of the recorded dLGN neurons were affected by CT FB suppression, 11% (13/122 neurons) by running, and 19% (23/122 neurons) by pupil size (**Figure 2f–h**, **Figure S4b–d**). The overall direction of modulation for the significant kernels aligned with the modulation indices obtained directly from the data (**Figure 1f**): CT FB

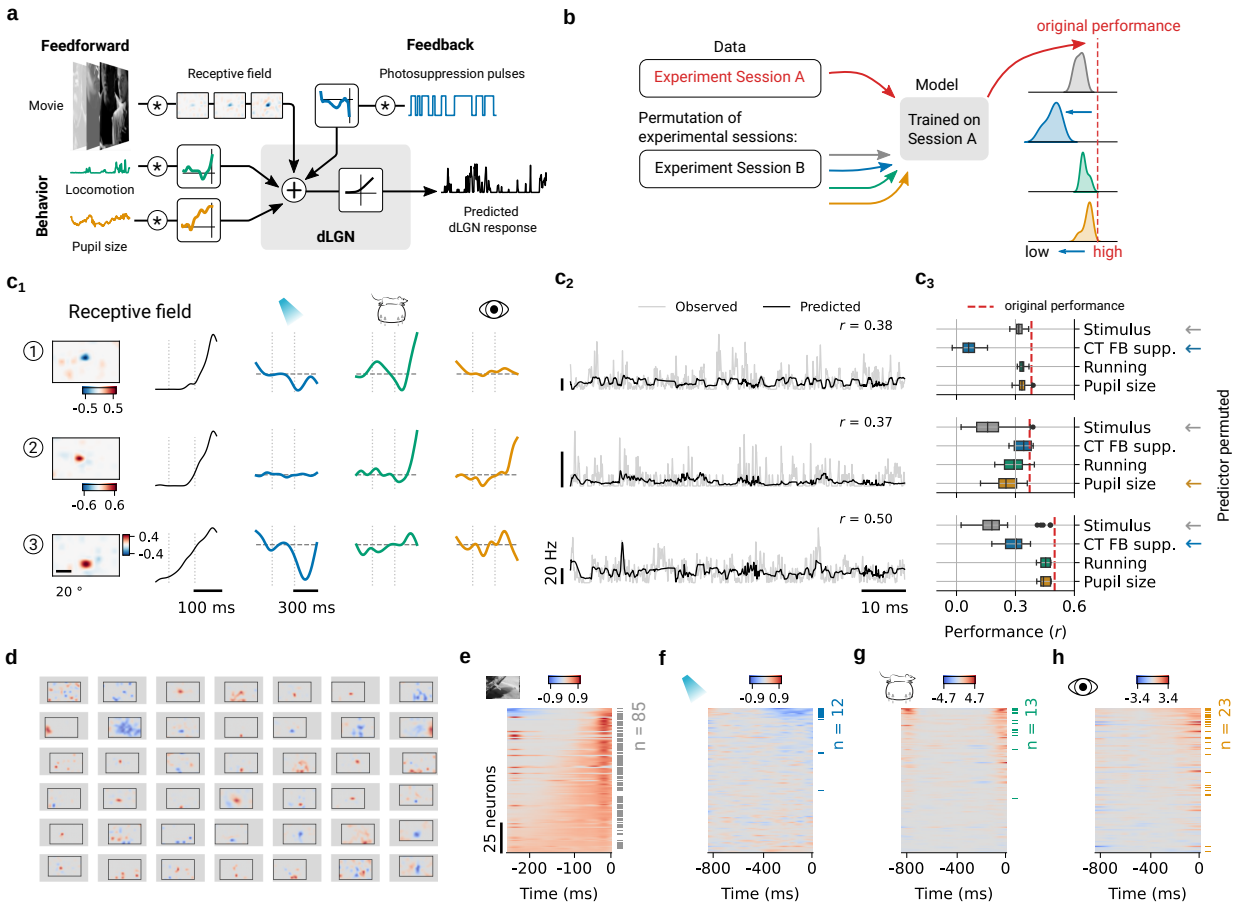


**Figure 2 | Spline-based GLM captured the receptive field, the influence of CT feedback and the impact of behaviour on responses of dLGN neurons.** (**a**) Schematics of the spline-GLM model architecture. dLGN firing rate was predicted as a combination of kernel outputs summed at the linear stage and then passed through a softplus nonlinearity. Each model neuron had a kernel for the stimulus, and three modulatory kernels for the non-retinal inputs: run speed (*green*), pupil size (*orange*), and CT FB suppression (*blue*). (**b**) Schematics of the permutation test (*51*) to evaluate the significance of the learned kernels. Model performance was evaluated by comparing the actual correlation (Pearson *r*) between predicted and observed firing rates to correlations when one of the inputs was taken from an unrelated experimental session (for movie, running, and pupil size) or randomly generated with the same statistics (for CT feedback suppression). (**c**) Three dLGN example neurons, their learned kernels, firing rate predictions, and outcomes of the permutation test (neuron 1 is the same example neuron as in **Figure 1d-e**). ($c_1$) Spatial and temporal RF components separated by singular value decomposition (SVD, see Methods), along with kernels for non-retinal inputs. ($c_2$) Observed (*gray*) versus predicted (*black*) ongoing firing rates. ($c_3$) Actual model performance (Pearson's *r*, *red*) and performance for permuted stimulus (*gray*), CT FB suppression (*blue*), running (*green*), and pupil size (*orange*) inputs. Kernels that contribute significantly to the model's performance are marked with ←. (**d**) Spatial RFs of example neurons with significant stimulus kernels. *Gray*: outline of common visual space (azimuth: -35–110 deg; elevation: -35–50 deg); *Solid lines*: monitor border. (**e**) Temporal RFs in the recorded dLGN population, sorted by their area under the curve (AUC). (**f**) Non-retinal kernels in the recorded dLGN population, sorted by their area under the curve. *Left to right:* Kernels for CT FB suppression, running, and pupil size. *Horizontal bars, side*: Neurons with significant kernels based on the permutation test.

suppression kernels were predominantly negative (**Figure 2f**), while running speed (**Figure 2g**) and pupil size (**Figure 2h**) kernels were predominantly positive. These results indicate that both CT feedback and behavioural state variables during natural movie viewing contribute to an overall increase of dLGN responses. Beyond the general sign of modulation, the learned model kernels also offered insights into the temporal dynamics of the non-retinal influences: consistent with the well-known slow impact of pupil dynamics on responses in the visual system (*47, 46*), we found that kernels for pupil size had a more sustained profile compared to kernels for running modulations (time to half max kernel running vs. pupil size: 106.31 ms vs. 146.27 ms, Wilcoxon signed-rank test: $p = 7.51 \times 10^{-3}$, **Figure S4l**). The ability to learn differential kernels demonstrates that our GLM model was successful in extracting the contributions of the various non-retinal inputs.

Despite the spline-GLM's overall success in predicting dLGN responses and learning biologically plausible kernels, it faced challenges in capturing fast modulations and response peaks, as typical also for traditional GLMs (*30, 55*). Theses challenges inherent in the GLM might have contributed to some spline artefacts near the left boundary of the learned kernels (**Figure 2e–h** and **Figure S4e–h**), in particular for the running kernels. This could be attributed to the fact that neurons modulated by running exhibited reduced response reliability (**Figure S5j**) and lower average firing rates (**Figure S5k**). Nevertheless, despite these challenges, the incorporation of running information proved beneficial for some neurons, as confirmed by the permutation test (**Figure S4c, g**).

Is the contribution of non-retinal inputs to dLGN neurons' activity consistent and strong enough to improve the prediction of dLGN responses? While dLGN has long been known to exhibit state-dependent changes in firing (*25, 27, 56*) and to receive extensive feedback from cortex (*57, 58*), the impact of these influences, in particular during viewing of naturalistic stimuli, is not well understood. Thus, to quantitatively assess the contributions of CT feedback suppression and behavioural variables, we compared the performance between our model including all inputs and reduced variants of the model with only a subset of inputs (**Figure 3a,b**). Starting with the 'Stimulus only' model that only considered the stimulus as input, we found that incorporating one or more non-retinal inputs increased the correlation between observed and predicted dLGN responses (ANOVA: $p = 0.022$; **Figure 3a**). In particular, adding pupil size or a combination of two or more predictors showed a significantly better performance than the 'Stimulus only' model ('Stimulus only' vs. 'Stimulus + Pupil size': 0.186 vs. 0.235, Wilcoxon signed-rank test: Bonferroni corrected $p = 3.39 \times 10^{-6}$; 'Stimulus only' vs. 'Full model': 0.186 vs. 0.249, Wilcoxon signed-rank test: Bonferroni corrected $p = 2.08 \times 10^{-7}$; **Figure 3a**). Note that even in the full model we still observe neurons with suboptimal predictions, likely due to low response reliability (**Figure S4i**) and low sparseness (**Figure S5e**).

Indeed, when we compared the prediction performance of the 'Stimulus-only' model with the 'Full model' (**Figure 3b**), we noticed that the inclusion of non-retinal inputs did not merely shift the distribution to higher performance. Instead, a closer examination allowed us to identify a sub-population of neurons whose responses could be predicted only poorly by the visual stimulus, but which profited strongly by the inclusion of the non-retinal factors (**Figure 3b–g**). These neurons also showed strong modulations by CT FB suppression (**Figure 3d**; **Figure S5a**), running (**Figure 3e**; **Figure S5b**), pupil size (**Figure 3f**; **Figure S5c**), or their combination (**Figure 3g**; **Figure S5d**).

Thus, our analysis of model performance suggests that dLGN neurons can be affected by non-retinal influences, albeit with considerable heterogeneity. Specifically, dLGN neurons seem to form at least two sub-populations: one strongly visually responsive sub-population with reliable responses across repeated visual stimuli, whose response prediction does not substantially improve by the addition of non-retinal inputs; and a second sub-population whose responses are less determined by the visual stimulus but instead are modulated by one or more non-retinal inputs. Similarly, the permutation test results supported the grouping of neurons into sub-populations according to the statistical significance to the retinal vs. non-retinal inputs (**Figure S5f**). Notably, previous studies have reported their success in identifying a visual response or a visual receptive field on the screen only for 60% (*59*), and 67% (*54*) of recorded dLGN neurons.

### CT feedback is enhanced in the absence of a patterned visual stimulus

Our model showed only a relatively small subset of dLGN neurons with significant effects of CT feedback. Could the reason for this be an interplay between feedforward and feedback signals within the dLGN? We hypothesised that the responses elicited by the rich naturalistic movie stimulus might have dominated dLGN activity relative to the effects of CT feedback, and thus predicted that CT feedback effects might be stronger without patterned stimulus input (**Figure 4a**).

To test this prediction, we expanded our analyses to the period of blank screen stimulation flanking the movie presentation, and compared the effects of CT feedback suppression in the recorded data and in models fit separately to responses during movies vs. blank periods (**Figure 4b**). Consistent with our prediction, we indeed observed that CT feedback suppression reduced the firing rates of individual example neurons more strongly during blanks ($MI_{opto}$: -0.65, **Figure 4c**$_1$) compared to movies ($MI_{opto}$: -0.45, **Figure 4c**$_2$). This observation held true across the recorded dLGN population (mean $MI_{opto}$, -0.09 vs. -0.03; $p = 2.5 \times 10^{-6}$, Wilcoxon signed-rank test; **Figure 4d**). Furthermore, during blank periods, more dLGN neurons were affected by the suppression of CT feedback (45% vs. 18% with $|MI_{opto}| \geq 0.1$; **Figure 4j**). The stronger effect of CT feedback suppression could not be explained by the difference in overall firing rate between the two stimulus conditions (**Figure S6a**),

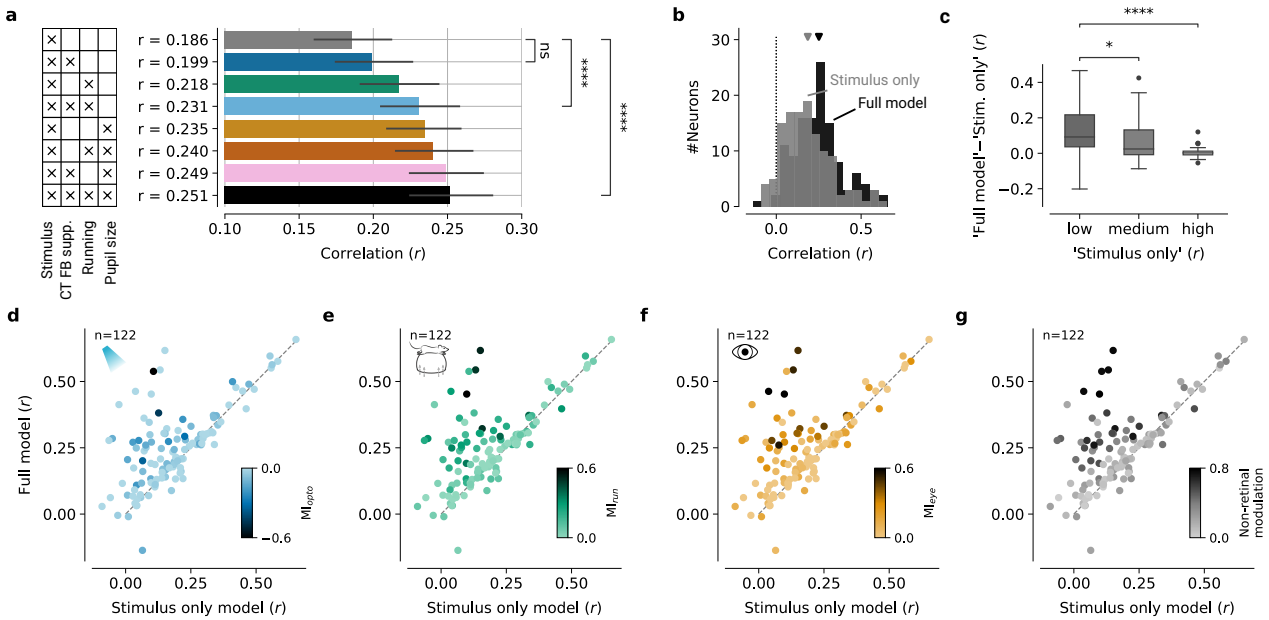


**Figure 3 | Adding non-retinal model predictors improves the performance in particular for a sub-population of poorly visually responsive dLGN neurons.** (**a**) Comparison of model performance for models with different sets of inputs indicated in table on the left, sorted by performance. Bonferroni corrected $p$-values of paired Wilcoxon signed-rank test: $****p \leq 1.0 \times 10^{-4}$; 'ns' non-significant. Error bars: 95% confidence intervals. (**b**) Comparison of model performance on the test set (Pearson's $r$) for the 'Full model' (*black*, inputs: stimulus, CT FB suppression, run speed, pupil size) and the 'Stimulus only' model (*gray*). *Arrow heads*: mean performance ($N = 122$ neurons). (**c**) Improvement in model performance observed with adding non-retinal predictors ('Full model'−'Stimulus only') for neurons grouped by their 'Stimulus only' performance. Bonferroni corrected $p$-values: $*p \leq 0.05$; $****p \leq 1.0 \times 10^{-}4$. (**d–f**) Comparison of model performances on the test set for all neurons in the 'Stimulus only' model and the 'Full model'. Darker colours indicate stronger modulation by CT feedback quantified by $MI_{opto}$ (d), by running quantified by $Mi_{Running}$ (e), and by pupil size quantified by $MI_{Eye}$ (f). (**g**) Same as in (d-f) but for $MI = 1-(1-MI_{Opto})(1-MI_{Run})(1-MI_{Eye})$ quantifying the joint modulation by non-retinal factors. Darker colours indicate stronger modulation by non-retinal variables.

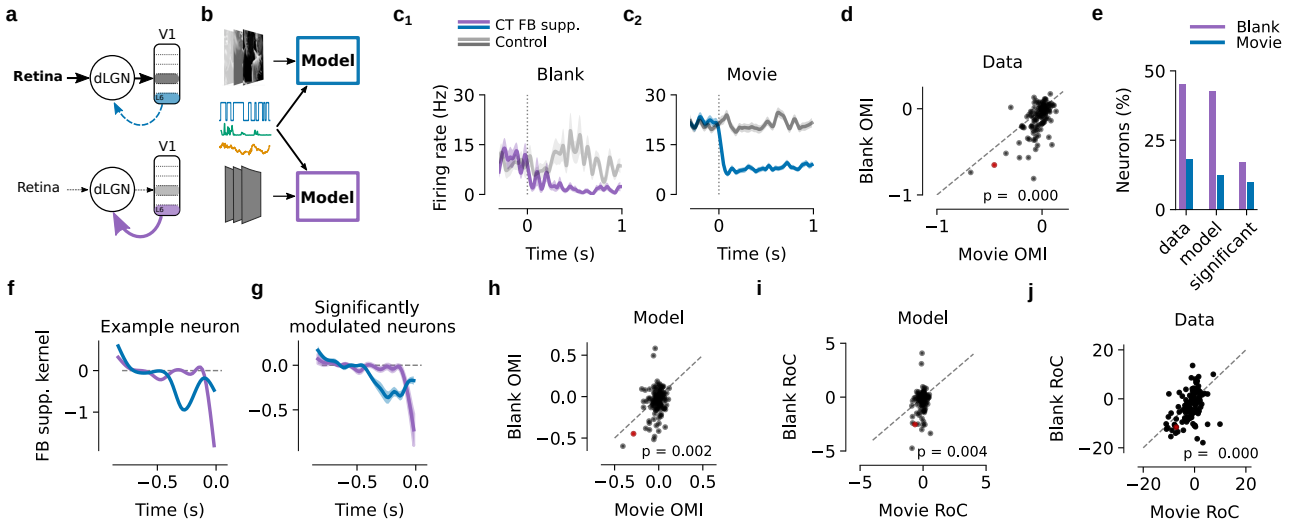


**Figure 4 | Strength of modulation by CT feedback is dependent on the presence or absence of the visual stimulus.** (**a**) Schematic illustration of the hypothesis that the absence of a patterned visual stimulus elicits weaker retinal feedforward input to dLGN, which is in turn accompanied by stronger CT feedback. (**b**) Schematics of fitting the spline-GLM model separately during movies *top* vs. blank periods *bottom*. (**c**$_1$) Mean PSTHs time locked to onset of photosuppression for one example dLGN neuron (same example neuron as in **Figure 1d-e**) during blank periods (gray screen) flanking the movie presentation. The shaded area represents the SEM. *Purple*: PSTH during CT feedback suppression, *light grey*: PSTH during control condition. (**c**$_2$) Same as (c$_1$), during movie presentation. *Blue*: PSTH during CT feedback suppression, *dark grey*: PSTH during control condition. (**d**) Comparison of $MI_{opto}$ during blanks vs. movies for the recorded dLGN population. (**e**) Percentage of recorded dLGN neurons modulated by CT feedback during the two stimulus conditions. Three modulation metrics were separately considered to count the modulated neurons. A neuron was considered modulated if (1) based on data: $|MI_{opto}|$ from (d) $\geq 0.1$, (2) based on model predictions: $|MI_{opto}|$ from (h) $\geq 0.1$, or (3) based on model performance: permutation test resulted in $p \leq 0.05$. Notably, all three modulation metrics consistently revealed a higher proportion of neurons displaying CT feedback modulation during the Blank condition compared to the movie condition. (**f**) CT feedback suppression kernel for the example dLGN neuron in (c$_1$). The model is either trained on the data from movie presentation (*dark blue*) or blank periods (*light blue*). Inset: simulated response of the same neuron using the Spline-GLM model to the two stimuli. (**g**) Same for all significantly CT feedback modulated neurons ($n_{movie}$ = 12, $n_{blank}$ = 21). Solid lines represent the mean of the kernels and transparent surrounds represent the standard error of the mean (SEM). (**h**) Comparison of $MI_{opto}$ for blanks vs. movies calculated from simulated data using the fitted model for the dLGN population to the two stimuli. (**i**) Comparison of the Rate of Change (RoC) of model-predicted neurons' responses to CT feedback suppression during movie presentation vs. blank periods. (**j**) Same as (i), for the recorded data.

nor was it related to the different number of optogenetic pulses (**Figure S6b**).

Is the stronger modulation by CT feedback suppression during blank periods vs. movies also captured by our modelling framework? We indeed found that the model learned a more negative CT feedback suppression kernel for the blank condition compared to the movie, both in example neurons (peak amplitude -1.8 vs. -0.94; **Figure 4f**) as well as in the population of neurons with a significant CT feedback suppression kernel (-0.86 vs. -0.46, $p = 0.044$, Mann-Whitney-U test, **Figure 4g**; all neurons: -0.4 vs. -0.2, $p = 5 \times 10^{-8}$, Wilcoxon signed-rank test). To avoid potential confounds of firing rates on kernel amplitudes (**Figure S6c,d**) and enable a more direct comparison to the recorded data, we used the model predictions in the two stimulus conditions and calculated model-derived $MI_{opto}$, analogously to those based on the recorded data. Consistent with our data-driven observations, we found that CT feedback suppression reduced modelled responses more strongly during the blank periods (modelled $MI_{opto}$, -0.057) compared to movies (-0.017; $p = 0.002$, Wilcoxon signed-rank test, **Figure 4h**).

Inspecting the learned model kernels **Figure 4f,g** suggested that, besides amplitude, the dynamics of the CT feedback suppression effects might also differ between visual stimulus conditions. Specifically, the spline-GLM learned a kernel characterised by a faster and briefer time course for blank periods compared to movie stimulation. This observation could be quantified by calculating the rate of change (RoC) of the neurons' predicted and actual responses after photosuppression (see Methods). Indeed, we found that the effect of CT feedback suppression was faster during blank periods (model-based RoC: $p = 0.004$, Wilcoxon signed-rank test, **Figure 4i**; data-based: $p = 9 \times 10^{-12}$, Wilcoxon signed-rank test,**Figure 4j**). In conclusion, the fitted spline-GLM models revealed that the impact of CT feedback suppression was weaker and slower during the presence of a rich patterned visual stimulus in comparison to blank periods, suggesting that the impact of CT feedback depends on the visual stimulus characteristics.

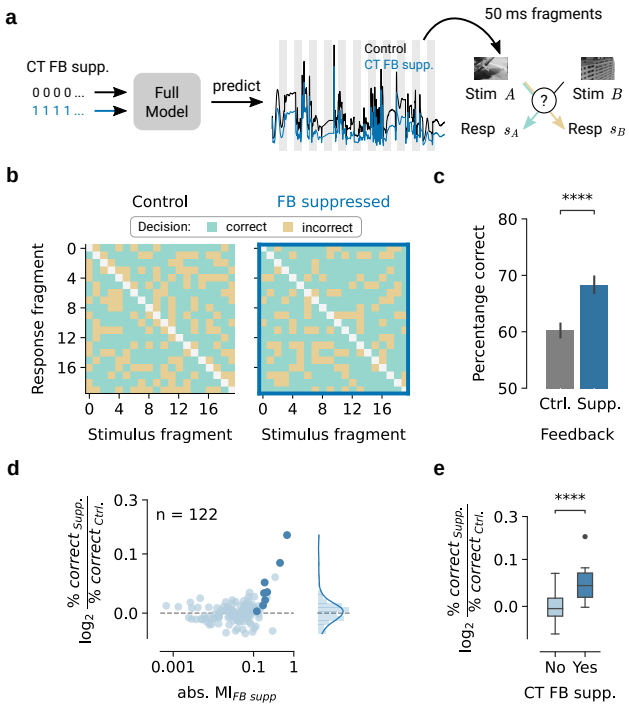


**Figure 5 | Two-alternative-forced-choice decoder shows better stimulus discrimination without feedback.** (**a**) Schematics of the decoder: the trained model was used to simulate responses with CT FB being either on (*blue*) or off (*black*; 70 s example trace). Random 50 ms stimulus fragments (*A* and *B*) were chosen, each with corresponding simulated responses. The decoder's task was to determine which stimulus was more likely based on the observed responses. (**b**) Decision matrix for one example neuron with 20 random stimulus fragments and their simulated responses. *Green*: correct pairing of stimulus and response; *Yellow*: incorrect pairing. *Left*: control condition; *right*: CT FB suppressed condition. (**c**) Percentage of correct decisions in the control and the CT FB suppressed condition, same example modelled neuron as in (b). Error bars indicate 95% confidence intervals. (**d**) Decoder performance across all neurons as a function of the amount of modulation by photosuppression observed in the experiment. *Dark blue*: neurons with a significant CT feedback kernel. (**e**) Relative decoder performance during CT FB suppression and control conditions, split according to whether neurons were significantly modulated by CT FB suppression (*dark blue*) or not modulated (*light blue*).

## CT feedback affects stimulus decoding

We finally sought to better understand if and how the suppression of CT feedback affected how dLGN encoded visual information (**Figure 5**). Specifically, we tested the degree to which suppression of CT feedback might affect the decoding of movie information based on the responses of single dLGN neurons, compared to the control condition where feedback was intact.

To address our question, we used the trained model ('Full model') to describe how individual dLGN neurons encode stimulus information (**Figure 5a**). In this way, we were able to isolate the effects of CT FB suppression *in silico*, by keeping stimulus, running and eye inputs intact, and only changing CT FB suppression (setting the CT FB input to either ON or OFF). We then performed a simple decoding experiment, using simulated model responses to discriminate between stimuli in a two-alternative forced choice (2AFC) setting (**Figure 5a**; (*35*)). We randomly selected 50 ms fragments of stimulus-response-pairs from the test set that had not been used for model fitting. To discriminate between two movie clips, we used the maximum-likelihood decoding rule from Pillow et al. (2005) (**Figure 5a**; see Methods). The decision of the 2AFC decoder was directly derived from the model likelihood for the correct and incorrect pairing (see Methods). We considered the 2AFC decoder to make a correct decision if the likelihood for the correct pairing was higher than for the incorrect one. We found that for an example neuron the decoder made more correct decisions in the FB suppressed condition compared to the control condition (**Figure 5b**, shown for 20 representative stimulus-response pairs; across all 100 stimulus pairs tested: 68.34 % vs. 60.27 %, $p = 1.20 \times 10^{-12}$, Wilcoxon rank sum test; **Figure 5c**).

To quantify the overall discrimination performance for each neuron, we computed the log ratio of the percent correct decoding performance in the FB suppressed condition over the percent correct in the control condition (**Figure 5d**). Positive log ratios indicate better decoding performance in the CT FB suppressed state. We observed log-ratios near zero, suggesting that for the majority of neurons there was no significant difference in stimulus information between control conditions and CT FB suppression on average (1.003±0.021, mean±SD; **Figure 5d**). However, we found significantly higher log-ratios in neurons modulated by CT FB compared to non-modulated neurons ($p = 5.84 \times 10^{-14}$, skew test against null; **Figure 5d right** and **Figure 5e**). Taken together, our model predicts that single trial responses of individual dLGN neurons are less informative about the visual stimulus with CT feedback intact. Given the strong convergence in the visual thalamocortical system and the exquisite sensitivity of thalamorecipient V1 neurons to temporally coordinated inputs (*60, 61*), the reduction of stimulus information in single trial - single neuron dLGN responses with CT feedback might be more than compensated by the increase in response strength, in particular for weak visual inputs (see also Discussion).

## Discussion

In this study we investigated how dLGN responses are influenced by the combination of feedforward inputs, CT feedback and behavioural state. Toward this end we modelled dLGN single neuron responses using a spline-based GLM with predictors for the visual stimulus, CT FB suppression, the animal's run speed, and pupil size. Our model identified a subpopulation of neurons whose responses were not well predicted by the visual input, yet for which the CT FB and behavioural inputs improved model performance. A comparison of our models trained on either naturalistic movies or blank periods revealed that the effect of CT FB was relatively stronger, more prevalent, and faster in the absence of a patterned visual stimulus. Finally, using Bayesian decoding, we found that the responses of a subset of CT-feedback-sensitive dLGN neurons contained more visual information when CT feedback was suppressed. Together, our results show that effects of non-retinal inputs in visual thalamus depend on visual responsiveness and stimulus context.

### Modulation of dLGN responses by non-retinal inputs

Despite sometimes being portrayed as a relay station, the dLGN of the thalamus has long been recognised as one of the earliest stages in the visual system that is modulated by extra-retinal inputs (*3, 25, 14, 9, 62*). In line with this notion, we found that performance of our model generally improved with the inclusion of non-retinal inputs, albeit with considerable neuron-by-neuron variability. Differential effects of behavioural state have been observed already in previous studies, where they been related to the visual feature selectivity of V1 neurons (*63*), dLGN neurons (*28*) or retinal boutons in dLGN (*29*). We extend this notion of differential modulations by non-retinal inputs in dLGN, showing that sub-populations of dLGN neurons whose responses were poorly predicted by the movie stimulus were more strongly affected by non-retinal inputs. The population of neurons in mouse dLGN with poor or unclear visual feature selectivity is not negligible, amounting to 30–40% (*59, 54*). Thus, studies of sensory processing that rely on selection criteria based on visual responsiveness might underestimate non-retinal response modulations in dLGN.

Our data-driven modulation indices generally matched well with the magnitudes of non-retinal modulations previously observed in mouse dLGN (*27, 28, 15, 12, 17*), yet we were surprised to see only a relatively small fraction of dLGN neurons with significant kernels for CT feedback, running and pupil size. There might be several reasons: first, session-based permutation tests are known to be conservative methods for assessing significant modulations (*51*), as they account for slow trends often present in neurophysiological signals that might otherwise inflate correlation-based metrics. Second, the data-driven modulation indices often reflect firing rates split into extreme conditions (e.g., locomotion slower than 0.25 cm/s considered as sitting but only faster than 1 cm/s is considered as running (*27, 28*)), while our model considered the predictor input on a continuum. Third, instead of recruiting powerful intracortical inhibition for suppression of CT feedback through photostimulation of inhibitory V1 neurons (*12, 11, 64, 15, 65, 16*), we chose a method of direct suppression of L6 CT feedback through the light-gated chloride channel stGtACR2 (*44*). Given the restriction of expression to the L6 somata located deep within cortex as a means for avoiding unwanted excitatory side effects, this form of photosuppression might be comparatively weaker than what has been applied in previous studies (see also (*15, 65*)).

### CT feedback effects on stimulus encoding and decoding

In contrast to previous studies reporting diverse effects of CT feedback that were often of opposing sign (*18*), we found that suppression of CT feedback resulted overall in a reduction of dLGN activity, and accordingly our model learned a negative CT FB suppression kernel for the significantly feedback-modulated neurons. Thus, at least during viewing of full-screen movie stimuli under head-fixed condition, the overall effect of CT FB seems to consist of an enhancement of dLGN responses. Furthermore, our results of faster and relatively stronger CT feedback effects during blank periods compared to movie viewing contribute to the growing knowledge that CT feedback effects seem to be stimulus-dependent, and partially overridden by visual stimulation (see also (*66, 15*)). Interestingly, CT feedback seems to be most potent in the absence of patterned stimulus input, both in mice (this study and (*67, 15*) for related findings with gratings) and ferrets (*66*), which might point to a common function across species. In addition, such stimulus-dependence might explain some of the variability of CT feedback effects observed across studies (also discussed in (*66*)). Future studies will need to use more subtle manipulations of stimulus strength to test the hypothesis that CT feedback might be most effective under challenging sensory conditions.

We observed that the decoding of visual stimulus information based on responses of the feedback-modulated neurons was enhanced during CT feedback suppression. This was surprising because previous research has linked effects of cortico-cortical feedback to attention (*68, 69*), which in visual areas is thought to enhance stimulus encoding (*70, 71*). What could be potential reasons why our model predicted improved decoding during CT feedback suppression? Past research has proposed that one role of CT feedback could be to linearize the input-output relationship of thalamic neurons through the injection of synaptic noise (*72, 73*). Under such synaptic noise, the firing of thalamic neurons can become less reliable, which might explain why our decoder operating on single stimulus segments performed more poorly with CT feedback intact. A shift towards more unreliable firing regimes by CT feedback would also be in line with our previous results (*15*), showing that CT feedback during

repeated movie segments increased the trial-by-trial variability of dLGN neurons' responses. Given the strong convergence of many dLGN neurons on individual V1 neurons (*60, 61*), a more realistic decoder would thus consider local populations of thalamocortical neurons, where synaptic noise mediated by CT feedback might allow to extract from the pooled afferent signal stimulus-related information with better resolution and with enhanced sensitivity to weaker inputs (*72, 73*).

### Spline-GLM for visual thalamic responses

Guided by previous work in the retina (*43*), we here used a spline-GLM to investigate the RF properties of dLGN neurons, and extended the model with inputs for behaviour and CT feedback. Using natural cubic splines as basis functions, we successfully estimated smooth RFs and non-retinal kernels. Furthermore, our GLM provided scale-ability by providing the option to incorporating multiple non-retinal inputs in addition to the stimulus. This enabled us to investigate the separate influences of various factors on dLGN responses. For instance, our model successfully recovered the differential modulation by correlated predictors, such as running speed and pupil size (*46, 47*). Specifically, the model captured fast modulation due to changes in locomotion speed and the gradual, smoother transitions due to pupil dilation or constriction (*47*).

GLMs have been previously applied to studying visual thalamic processing of artificial and naturalistic stimuli, with most of these previous studies being performed in anaesthetised cats (e.g., (*74, 42, 41*)). Particularly relevant in this context is the work of Babadi et al. (2010) (*41*), who reported that incorporating "indirect visual input" in their GLM, potentially representing CT feedback effects, improved prediction quality, in particular for stimulus sizes that exceeded the classical RF size (*41*). In line with our results, the amount of improvement varied across neurons.

### Estimating receptive fields with extended spline-GLM

In addition to recovering the impact of non-retinal inputs on dLGN activity, our modelling framework allowed us to relate the learned RF kernels to known response properties in mouse dLGN. Consistent with previous studies quantifying dLGN RFs in the mouse to simple stimuli (*50, 54, 53, 52*), our model learned, for many dLGN neurons, circular spatial RFs, which often consisted of a single domain resembling the well known ON and OFF fields. As has been noted before (*50, 54*), fewer dLGN neurons also had an opposing surround. In addition to these classical RF types, significant stimulus-related kernels to our movie stimulus also exhibited distributed and complex spatial RFs with multiple activation peaks or elongated shapes. One possibility could be that the rich visual movie stimulus used in our study for obtaining RF maps allowed unveiling selectivity for complex spatial features in mouse dLGN, akin to the complex feature selectivities recently discovered with natural scenes for mouse V1 (*75*).

Overall, the model mirrored both the spatial polarity and the temporal dynamics of known dLGN functional cell types, which were identified through clustering the neurons' responses to full-field luminance steps. However, we observed several neurons that exhibited a reversal in the polarity of their receptive field centres between the two visual stimuli. This observation might be attributed to a potential stimulus/context-dependent selectivity of dLGN neurons. Similar stimulus-dependent selectivity was reported in V1 (*59*), and a recent study has also shown that retinal neurons can reverse the polarity of their receptive fields in response to different natural images (*76*).

### Limitations of the model and future extensions

While our GLM with spline-basis allowed us to capture dLGN responses with biologically interpretable kernels, it also comes with several limitations. Non-retinal modulations have in the past often been linked to gain changes (locomotion: (*77, 27, 28, 46*); pupil size changes: (*46*); CT feedback: (*15*)), which would justify deviating from our GLM framework in two ways: (1) by employing a multiplication instead of a summation to integrate the predictors, and (2) by using an exponential nonlinearity (since mathematically exponentiating the summed kernel responses is equivalent to modelling them as multiplicative influences on neural activity (*31*)). However, for a multiplicative versions of the model, we encountered compensatory effects that obscured the interpretability of the kernel shape. Furthermore, the use of an exponential nonlinearity lead to highly unstable behaviour of the loss during model training. But even if the multiplicative behaviour of the predictors were accommodated by the model, this would still not address any sharpening of orientation selectivity, as reported for effects of pupil dilation on V1 orientation tuning curves (*46*), and the known changes in spatial integration of dLGN neurons driven by CT feedback (*21, 12*).

In the future, there are a number of possible extensions of our spline-GLM. First, instead of considering the spatio-temporal RF fixed, the model could contain mechanisms for fast adaptation of gain and integration time according to luminance and contrast (*78, 74*), accounting for the constant changes in spatial and temporal integration elicited by dynamic natural stimuli. This could be achieved by creating additional predictors that represented a combination of e.g. stimulus intensity and CT FB suppression. Second, CT feedback could be modelled as a spatio-temporal kernel instead of a single gain factor, accounting for the well-known differential effects of CT feedback on spatial integration (*21, 12*). Third, the model could be used to test interactions between CT feedback effects and behavioural state-related modulations, as proposed by some studies (*65*). Finally, an important nonlinear feature of thalamic responses are bursts, which are thought to be related not only to the behavioural state of the animal (*77, 25, 27*) and CT feedback (*15*), but can also be triggered by features of natural stimuli (*79*). Different model

architectures will be needed to include this nonlinear response feature of thalamic neurons.

In conclusion, our results add to the growing body of evidence that dLGN activity is influenced not only by retinal visual inputs but also non-retinal influences from CT feedback and behavioural state. While our model is purely phenomenological (*31, 33*), this work presents an important step towards a quantitative understanding of how dLGN responses to complex, naturalistic stimuli are shaped by the simultaneous influences of retinal feedforward inputs, CT feedback and behaviour.

## References


1. W. Guido, Development, form, and function of the mouse visual thalamus. *Journal of Neurophysiology* **120**, 211–225 (2018).
2. W. M. Usrey, H. J. Alitto, Visual Functions of the Thalamus. *Annual Review of Vision Science* **1**, 351–371 (2015).
3. T. G. Weyand, The multifunctional lateral geniculate nucleus. *Reviews in the Neurosciences* **27**, 135–157 (2016).
4. M. Román Rosón, Y. Bauer, A. Kotkat, P. Berens, T. Euler, L. Busse, Mouse dLGN Receives Functional Input from a Diverse Population of Retinal Ganglion Cells with Limited Convergence. *Neuron* **102**, 462–476 (2019).
5. J. L. Morgan, D. R. Berger, A. W. Wetzel, J. W. Lichtman, The Fuzzy Logic of Network Connectivity in Mouse Visual Thalamus. *Cell* **165**, 192–206 (2016).
6. S. Hammer, A. Monavarfeshani, T. Lemon, J. Su, M. A. Fox, Multiple Retinal Axons Converge onto Relay Cells in the Adult Mouse Thalamus. *Cell Reports* **12**, 1575–1583 (2015).
7. L. Liang, A. Fratzl, G. Goldey, R. N. Ramesh, A. U. Sugden, J. L. Morgan, C. Chen, M. L. Andermann, A fine-scale functional logic to convergence from retina to thalamus. *Cell* **173**, 1343–1355.e24 (2018).
8. J. A. Hirsch, X. Wang, F. T. Sommer, L. M. Martinez, How inhibitory circuits in the thalamus serve vision. *Annual Review of Neuroscience* **38**, 309–329 (2015).
9. A. M. Sillito, J. Cudeiro, H. E. Jones, Always returning: feedback and sensory processing in visual cortex and thalamus. *Trends in Neurosciences* **29**, 307–316 (2006).
10. F. Briggs, W. M. Usrey, Corticogeniculate feedback and parallel processing in the primate visual system. *Journal of Physiology* **589**, 33–40 (2011).
11. S. R. Olsen, D. S. Bortone, H. Adesnik, M. Scanziani, Gain control by layer six in cortical circuits of vision. *Nature* **483**, 47–52 (2012).
12. G. Born, F. A. Schneider-Soupiadis, S. Erisken, A. Vaiceliunaite, C. L. Lao, M. H. Mobarhan, M. A. Spacek, G. T. Einevoll, L. Busse, Corticothalamic feedback sculpts visual spatial integration in mouse thalamus. *Nature Neuroscience* **24**, 1711–1720 (2021).
13. G. M. G. Shepherd, N. Yamawaki, Untangling the cortico-thalamo-cortical loop: cellular pieces of a knotty circuit puzzle. *Nature Reviews Neuroscience* **22**, 389–406 (2021).
14. D. A. McCormick, Neurotransmitter actions in the thalamus and cerebral cortex and their role in neuromodulation of thalamocortical activity. *Progress in Neurobiology* **39**, 337–388 (1992).
15. M. A. Spacek, D. Crombie, Y. Bauer, G. Born, X. Liu, S. Katzner, L. Busse, Robust effects of corticothalamic feedback and behavioral state on movie responses in mouse dlgn. *Elife* **11**, e70469 (2022).
16. D. B. Nestvogel, D. A. McCormick, Visual thalamocortical mechanisms of waking state-dependent activity and alpha oscillations. *Neuron* **110**, 120–138.e4 (2022).
17. B. Molnár, P. Sere, S. Bordé, K. Koós, N. Zsigri, P. Horváth, M. L. Lőrincz, Cell Type-Specific Arousal-Dependent Modulation of Thalamic Activity in the Lateral Geniculate Nucleus. *Cerebral Cortex Communications* **2**, tgab020 (2021).
18. D. J. Denman, D. Contreras, Complex effects on in vivo visual responses by specific projections from mouse cortical layer 6 to dorsal lateral geniculate nucleus. *The Journal of Neuroscience* **35**, 9265–80 (2015).
19. F. Briggs, Role of feedback connections in central visual processing. *Annual Review of Vision Science* **6**, 313–334 (2020).
20. J. W. McClurkin, R. T. Marrocco, Visual cortical input alters spatial tuning in monkey lateral geniculate nucleus cells. *The Journal of Physiology* **348**, 135–152 (1984).
21. P. C. Murphy, A. M. Sillito, Corticofugal feedback influences the generation of length tuning in the visual pathway. *Nature* **329**, 727–729 (1987).
22. H. E. Jones, I. M. Andolina, B. Ahmed, S. D. Shipp, J. T. C. Clements, K. L. Grieve, J. Cudeiro, T. E. Salt, A. M. Sillito, Differential feedback modulation of center and surround mechanisms in parvocellular cells in the visual thalamus. *The Journal of Neuroscience* **32**, 15946–15951 (2012).
23. J. M. Hasse, F. Briggs, Corticogeniculate feedback sharpens the temporal precision and spatial resolution of visual signals in the ferret. *Proceedings of the National Academy of Sciences of the United States of America* **114**, E6222–E6230 (2017).

**24.** H. A. Swadlow, T. G. Weyand, Corticogeniculate neurons, corticotectal neurons, and suspected interneurons in visual cortex of awake rabbits: receptive-field properties, axonal properties, and effects of EEG arousal. *Journal of Neurophysiology* **57**, 977–1001 (1987).

**25.** T. Bezdudnaya, M. Cano, Y. Bereshpolova, C. R. Stoelzel, J.-M. Alonso, H. A. Swadlow, Thalamic burst mode and inattention in the awake LGNd. *Neuron* **49**, 421–432 (2006).

**26.** M. Cano, T. Bezdudnaya, H. A. Swadlow, J.-M. Alonso, Brain state and contrast sensitivity in the awake visual thalamus. *Nature Neuroscience* **9**, 1240–1242 (2006).

**27.** S. Erisken, A. Vaiceliunaite, O. Jurjut, M. Fiorini, S. Katzner, L. Busse, Effects of locomotion extend throughout the mouse early visual system. *Current Biology* **24**, 2899–2907 (2014).

**28.** Ç. Aydın, J. Couto, M. Giugliano, K. Farrow, V. Bonin, Locomotion modulates specific functional cell types in the mouse visual thalamus. *Nature communications* **9**, 4882 (2018).

**29.** L. Liang, A. Fratzl, J. D. Reggiani, O. E. Mansour, C. Chen, M. L. Andermann, Retinal inputs to the thalamus are selectively gated by arousal. *Current Biology* **30**, 3923–3934.e9 (2020).

**30.** L. Paninski, Maximum likelihood estimation of cascade point-process neural encoding models. *Network: Computation in Neural Systems* **15**, 243–262 (2004).

**31.** J. W. Pillow, J. Shlens, L. Paninski, A. Sher, A. M. Litke, E. J. Chichilnisky, E. P. Simoncelli, Spatio-temporal correlations and visual signalling in a complete neuronal population. *Nature* **454**, 995–999 (2008).

**32.** J.-M. Lueckmann, J. H. Macke, H. Nienborg, Can serial dependencies in choices and neural activity explain choice probabilities? *Journal of Neuroscience* **38**, 3495–3506 (2018).

**33.** D. A. Butts, Data-driven approaches to understanding visual neuron activity. *Annual Review of Vision Science* **5**, 451–477 (2019).

**34.** L. Paninski, J. Pillow, J. Lewi, Statistical models for neural encoding, decoding, and optimal stimulus design. *Progress in Brain Research* (Elsevier, 2007), pp. 493–507.

**35.** J. W. Pillow, L. Paninski, V. J. Uzzell, E. P. Simoncelli, E. J. Chichilnisky, Prediction and decoding of retinal ganglion cell responses with a probabilistic spiking model. *Journal of Neuroscience* **25**, 11003–11013 (2005).

**36.** N. A. Steinmetz, P. Zatka-Haas, M. Carandini, K. D. Harris, Distributed coding of choice, action and engagement across the mouse brain. *Nature* **576**, 266–273 (2019).

**37.** C. A. Runyan, E. Piasini, S. Panzeri, C. D. Harvey, Distinct timescales of population coding across cortex. *Nature* **548**, 92–96 (2017).

**38.** I. M. Park, M. L. R. Meister, A. C. Huk, J. W. Pillow, Encoding and decoding in parietal cortex during sensorimotor decision-making. *Nature Neuroscience* **17**, 1395–1403 (2014).

**39.** S. Musall, M. T. Kaufman, A. L. Juavinett, S. Gluf, A. K. Churchland, Single-trial neural dynamics are dominated by richly varied movements. *Nature Neuroscience* **22**, 1677–1686 (2019).

**40.** P. M. Goltstein, S. Reinert, T. Bonhoeffer, M. Hübener, Mouse visual cortex areas represent perceptual and semantic features of learned visual categories. *Nature Neuroscience* **24**, 1441–1451 (2021).

**41.** B. Babadi, A. Casti, Y. Xiao, E. Kaplan, L. Paninski, A generalized linear model of the impact of direct and indirect inputs to the lateral geniculate nucleus. *Journal of Vision* **10**, 22–22 (2010).

**42.** D. A. Butts, C. Weng, J. Jin, J.-M. Alonso, L. Paninski, Temporal precision in the visual pathway through the interplay of excitation and stimulus-driven suppression. *Journal of Neuroscience* **31**, 11313–11327 (2011).

**43.** Z. Huang, Y. Ran, J. Oesterle, T. Euler, P. Berens, Estimating smooth and sparse neural receptive fields with a flexible spline basis. *Neurons, Behavior, Data analysis, and Theory* **8**, 1–14 (2021).

**44.** M. Mahn, L. Gibor, P. Patil, K. Cohen-Kashi Malina, S. Oring, Y. Printz, R. Levy, I. Lampl, O. Yizhar, High-efficiency optogenetic silencing with soma-targeted anion-conducting channelrhodopsins. *Nature communications* **9**, 4125 (2018).

**45.** S. Gong, M. Doughty, C. R. Harbaugh, A. Cummins, M. E. Hatten, N. Heintz, C. R. Gerfen, Targeting Cre Recombinase to Specific Neuron Populations with Bacterial Artificial Chromosome Constructs. *Journal of Neuroscience* **27**, 9817–9823 (2007).

**46.** J. Reimer, E. Froudarakis, C. R. Cadwell, D. Yatsenko, G. H. Denfield, A. S. Tolias, Pupil Fluctuations Track Fast Switching of Cortical States during Quiet Wakefulness. *Neuron* **84**, 355–362 (2014).

**47.** M. Vinck, R. Batista-Brito, U. Knoblich, J. A. Cardin, Arousal and Locomotion Make Distinct Contributions to Cortical Activity Patterns and Visual Encoding. *Neuron* **86**, 740–754 (2015).

**48.** G. Felsen, Y. Dan, A natural approach to studying vision. *Nature Neuroscience* **8**, 1643–1646 (2005).

**49.** P. R. Parker, E. T. Abe, E. S. Leonard, D. M. Martins, C. M. Niell, Joint coding of visual input and eye/head position in V1 of freely moving mice. *Neuron* p. S0896627322008042 (2022).

**50.** D. M. Piscopo, R. N. El-Danaf, a. D. Huberman, C. M. Niell, Diverse Visual Features Encoded in Mouse Lateral Geniculate Nucleus. *Journal of Neuroscience* **33**, 4642–4656 (2013).

**51.** K. D. Harris, Nonsense correlations in neuroscience. *bioRxiv* pp. 1–13 (2020).

**52.** S. Durand, R. Iyer, K. Mizuseki, S. De Vries, S. Mihalas, R. C. Reid, A comparison of visual response properties in the lateral geniculate nucleus and primary visual cortex of awake and anesthetized mice. *Journal of Neuroscience* **36**, 12144–12156 (2016).

**53.** J. Tang, S. C. A. Jimenez, S. Chakraborty, S. R. Schultz, Visual receptive field properties of neurons in the mouse lateral geniculate nucleus. *PLOS ONE* **11**, e0146017 (2016).

**54.** M. S. Grubb, I. D. Thompson, Quantitative characterization of visual response properties in the mouse dorsal lateral geniculate nucleus. *Journal of neurophysiology* **90**, 3594–3607 (2003).

**55.** B. A. Olshausen, D. J. Field, How close are we to understanding v1? *Neural computation* **17**, 1665–1699 (2005).

**56.** C. M. Niell, M. P. Stryker, Modulation of visual responses by behavioral state in mouse visual cortex. *Neuron* **65**, 472–479 (2010).

**57.** A. M. Sillito, H. E. Jones, Corticothalamic interactions in the transfer of visual information. *Philosophical Transactions of the Royal Society of London. Series B: Biological Sciences* **357**, 1739–1752 (2002).

**58.** F. Briggs, W. M. Usrey, Corticogeniculate feedback and visual processing in the primate. *Journal of Physiology* **589**, 33–40 (2010).

**59.** J. H. Siegle, X. Jia, S. Durand, S. Gale, C. Bennett, N. Graddis, G. Heller, T. K. Ramirez, H. Choi, J. A. Luviano, *et al.*, Survey of spiking in the mouse visual system reveals functional hierarchy. *Nature* **592**, 86–92 (2021).

**60.** W. M. Usrey, J. B. Reppas, R. C. Reid, Paired-spike interactions and synaptic efficacy of retinal inputs to the thalamus. *Nature* **395**, 384–387 (1998).

**61.** J.-M. Alonso, W. M. Usrey, R. C. Reid, Precisely correlated firing in cells of the lateral geniculate nucleus. *Nature* **383**, 815–819 (1996).

**62.** S. M. Sherman, R. W. Guillery, The role of the thalamus in the flow of information to the cortex. *Philosophical transactions of the Royal Society of London* **357**, 1695–708 (2002).

**63.** P. J. Mineault, E. Tring, J. T. Trachtenberg, D. L. Ringach, Enhanced Spatial Resolution During Locomotion and Heightened Attention in Mouse Primary Visual Cortex. *Journal of Neuroscience* **36**, 6382–6392 (2016).

**64.** J. Kim, C. J. Matney, A. Blankenship, S. Hestrin, S. P. Brown, Layer 6 corticothalamic neurons activate a cortical output layer, layer 5a. *J Neurosci* **34**, 9656–9664 (2014).

**65.** K. Reinhold, A. Resulaj, M. Scanziani, Brain state-dependent modulation of thalamic visual processing by cortico-thalamic feedback. *The Journal of Neuroscience* **43**, 1540–1554 (2023).

**66.** S. Zhu, J. Hasse, F. Briggs, Optogenetic suppression of corticogeniculate feedback in anesthetized ferrets is overridden by visual stimulation. *bioRxiv* (2021).

**67.** M. A. Kirchgessner, A. D. Franklin, E. M. Callaway, Distinct "driving" versus "modulatory" influences of different visual corticothalamic pathways. *Current Biology* **31**, 5121–5137 (2021).

**68.** P. R. Roelfsema, F. P. de Lange, Early visual cortex as a multiscale cognitive blackboard. *Annual review of vision science* **2**, 131–151 (2016).

**69.** V. A. Lamme, P. R. Roelfsema, The distinct modes of vision offered by feedforward and recurrent processing. *Trends in neurosciences* **23**, 571–579 (2000).

**70.** J. L. Herrero, M. A. Gieselmann, M. Sanayei, A. Thiele, Attention-induced variance and noise correlation reduction in macaque v1 is mediated by nmda receptors. *Neuron* **78**, 729–739 (2013).

**71.** A. Thiele, Optimizing brain processing. *Nature neuroscience* **12**, 1359–1360 (2009).

**72.** S. Béhuret, C. Deleuze, T. Bal, Corticothalamic synaptic noise as a mechanism for selective attention in thalamic neurons. *Frontiers in Neural Circuits* **9**, 80 (2015).

**73.** J. Wolfart, D. Debay, G. Le Masson, A. Destexhe, T. Bal, Synaptic background activity controls spike transfer from thalamus to cortex. *Nature neuroscience* **8**, 1760–1767 (2005).

**74.** N. A. Lesica, J. Jin, C. Weng, C.-i. Yeh, D. A. Butts, G. B. Stanley, J.-m. Alonso, Adaptation to stimulus contrast and correlations during natural visual stimulation. *Neuron* **55**, 479–491 (2007).

**75.** E. Y. Walker, F. H. Sinz, E. Cobos, T. Muhammad, E. Froudarakis, P. G. Fahey, A. S. Ecker, J. Reimer, X. Pitkow, A. S. Tolias, Inception loops discover what excites neurons most using deep predictive models. *Nature Neuroscience* **22**, 2060–2065 (2019).

**76.** M. A. Goldin, B. Lefebvre, S. Virgili, M. K. Pham Van Cang, A. Ecker, T. Mora, U. Ferrari, O. Marre, Context-dependent selectivity to natural images in the retina. *Nature Communications* **13**, 5556 (2022).

**77.** C. M. Niell, M. P. Stryker, Modulation of Visual Responses by Behavioral State in Mouse Visual Cortex. *Neuron* **65**, 472–479 (2010).

**78.** V. Mante, V. Bonin, M. Carandini, Functional Mechanisms Shaping Lateral Geniculate Responses to Artificial and Natural Stimuli. *Neuron* **58**, 625–638 (2008).

**79.** N. A. Lesica, G. B. Stanley, Encoding of natural scene movies by tonic and burst spikes in the lateral geniculate nucleus. *Journal of Neuroscience* **24**, 10731–10740 (2004).

**80.** J. Wietek, S. Rodriguez-Rozada, J. Tutas, F. Tenedini, C. Grimm, T. G. Oertner, P. Soba, P. Hegemann, J. Simon Wiegert, Anion-conducting channelrhodopsins with tuned spectra and modified kinetics engineered for optogenetic manipulation of behavior. *Scientific Reports* **7**, 1–18 (2017).

**81.** E. G. Govorunova, O. A. Sineshchekov, R. Janz, X. Liu, J. L. Spudich, Natural light-gated anion channels: A family of microbial rhodopsins for advanced optogenetics. *Science* **349**, 647–650 (2015).

**82.** L. Madisen, T. A. Zwingman, S. M. Sunkin, S. W. Oh, A. Hatim, H. Gu, L. L. Ng, R. D. Palmiter, M. J. Hawrylycz, R. Allan, E. S. Lein, H. Zeng, A robust and high-throughput Cre reporting and characterization system for the whole mouse brain. *Nature neuroscience* **13**, 133–140 (2010).

**83.** Z. Josh Huang, H. Zeng, Z. J. Huang, H. Zeng, Genetic Approaches to Neural Circuits in the Mouse. *Annual review of neuroscience* **36**, 183–215 (2013).

**84.** D. S. Bortone, S. R. Olsen, M. Scanziani, Translaminar inhibitory cells recruited by layer 6 corticothalamic neurons suppress visual cortex. *Neuron* **82**, 474–485 (2014).

**85.** J. E. Frandolig, C. J. Matney, K. Lee, J. Kim, M. Chevée, S.-J. Kim, A. A. Bickert, S. P. Brown, The Synaptic Organization of Layer 6 Circuits Reveals Inhibition as a Major Output of a Neocortical Sublamina. *Cell Reports* **28**, 3131–3143 (2019).

**86.** M. Mahn, M. Prigge, S. Ron, R. Levy, O. Yizhar, Biophysical constraints of optogenetic inhibition at presynaptic terminals. *Nature Neuroscience* (2016).

**87.** J. S. Wiegert, T. G. Oertner, How (not) to silence long-range projections with light. *Nature Neuroscience* **19**, 527–528 (2016).

**88.** J. S. Wiegert, M. Mahn, M. Prigge, Y. Printz, O. Yizhar, Silencing Neurons: Tools, Applications, and Experimental Constraints. *Neuron* **95**, 504–529 (2017).

**89.** C. A. Poynton, *Human Vision and Electronic Imaging III*, B. E. Rogowitz, T. N. Pappas, eds. (International Society for Optical Engineering, San Jose, CA, 1998), vol. 3299, pp. 232–249.

**90.** C. T. Rueden, J. Schindelin, M. C. Hiner, B. E. DeZonia, A. E. Walter, E. T. Arena, K. W. Eliceiri, ImageJ2: ImageJ for the next generation of scientific image data. *BMC Bioinf.* **18** (2017).

**91.** J. Schindelin, I. Arganda-Carreras, E. Frise, V. Kaynig, M. Longair, T. Pietzsch, S. Preibisch, C. Rueden, S. Saalfeld, B. Schmid, J.-Y. Tinevez, D. J. White, V. Hartenstein, K. Eliceiri, P. Tomancak, A. Cardona, Fiji: An open-source platform for biological-image analysis. *Nat. Methods* **9**, 676-682 (2012).

**92.** M. Pachitariu, N. Steinmetz, S. Kadir, M. Carandini, K. D. Harris, Kilosort: realtime spike-sorting for extracellular electrophysiology with hundreds of channels. *bioRxiv* p. 061481 (2016).

**93.** M. A. Spacek, T. J. Blanche, N. V. Swindale, Python for large-scale electrophysiology. *Front. Neuroinform.* **2**, 9 (2009).

**94.** N. V. Swindale, M. A. Spacek, Spike sorting for polytrodes: A divide and conquer approach. *Frontiers in Systems Neuroscience* (2014).

**95.** D. Yatsenko, E. Y. Walker, A. S. Tolias, DataJoint: A simpler relational data model (2018).

**96.** M. Sahani, J. F. Linden, Evidence optimization techniques for estimating stimulus-response functions. *Advances in neural information processing systems* pp. 317–324 (2003).

**97.** M. Park, J. W. Pillow, Receptive field inference with localized priors. *PLoS computational biology* **7**, e1002219 (2011).

**98.** W. E. Vinje, J. L. Gallant, Sparse coding and decorrelation in primary visual cortex during natural vision. *Science* **287**, 1273–1276 (2000).

## Acknowledgements

This research was supported by the Deutsche Forschungsgesellschaft (DFG) Sonderforschungsbereich (SFB) 1233, *Robust Vision: Inference Principles and Neural Mechanisms*, Teilprojekt (TP) 13, project number: 276693517 (L.B., P.B.), by SPP2041 (BU 1808/6-1 and BU 1808/6-2), the RTG 2175 "Perception in context and its neural basis" and the Hertie Foundation. Lisa Schmors was supported by the International Max Planck Research School for Intelligent Systems (IMPRS-IS). We thank E. Froudarakis (A. Tolias Lab, Baylor College of Medicine, Houston, TX) for providing of the movie stimulus files, S. Renner for helping with the database implementation, and A. Ecker and T. Euler for discussion of the stimulus design. Thanks also go to M. Sotgia for lab management and support with animal handling and histology, S. Schörnich for IT support, and B. Grothe for providing excellent research infrastructure.

## Author contributions

Conceptualization, L.B., P.B., S.S.; Methodology, L.S., Y.B., A.K., Z.H., D.C. P.B., S.S., L.B.; Software, L.S., A.K., Y.B., Z.H., D.C.; Formal Analysis, L.S., A.K., Y.B.; Investigation, Y.B., A.K., L.M.; Resources, L.B., P.B.; Data Curation, L.S., A.K., Y.B., L.M., D.C.; Writing – Original Draft, L.B., L.S., A.K., Y.B.; Writing – Review & Editing, all authors; Visualization, L.S., A.K., Y.B.; Supervision, L.B., P.B., S.S.; Project Administration, L.B., P.B.; Funding Acquisition, L.B., P.B.

## Declaration of Interests

The authors declare no competing interests.

## Data and code availability

Data and code will be made available upon submission.

## Methods

All procedures complied with the European Communities Council Directive 2010/63/EU and the German Law for Protection of Animals, and were approved by local authorities, following appropriate ethics review.

### Surgical procedures

Experiments were carried out under under Licence ROB-55.2-2532.Vet_02-17-40 in 4 adult Ntsr1-Cre mice (median age: 16.4 weeks; B6.FVB(Cg)-Tg(Ntsr1-cre)GN220Gsat/Mmcd; MMRRC) of either sex.

Stereotactic surgeries were performed to implant a head-post for head-fixation, implant a ground/reference screw for electrophysiology, inject a virus for optogenetic feedback manipulation, and drill a craniotomy for acute electrode insertions.

#### *Stereotactic surgery preparation and initiation*

Thirty minutes prior to the surgical procedure, mice were injected with an analgesic (Metamizole, 200 mg/kg, sc, MSD Animal Health, Brussels, Belgium). To induce anesthesia, animals were placed in an induction chamber and exposed to isoflurane (5% in oxygen, CP-Pharma, Burgdorf, Germany). After induction of anesthesia, mice were fixated in a stereotaxic frame (Drill & Microinjection Robot, Neurostar, Tuebingen, Germany) and the isoflurane level was lowered (0.5 %–2 % in oxygen), such that a stable level of anesthesia could be achieved as judged by the absence of an interstitial reflex. Throughout the procedure, the eyes were covered with an eye ointment (Bepanthen, Bayer, Leverkusen, Germany) and a closed loop temperature control system (ATC 1000, WPI Germany, Berlin, Germany) ensured that the animal's body temperature was maintained at 37° C. At the beginning of the surgical procedure, an additional analgesic was administered (Buprenorphine, 0.1 mg/kg, sc, Bayer,

Leverkusen, Germany) and the animal's head was shaved and thoroughly disinfected using iodine solution (Braun, Melsungen, Germany). Before performing a scalp incision along the midline, a local analgesic was delivered (Lidocaine hydrochloride, sc, bela-pharm, Vechta, Germany). The skin covering the skull was partially removed and cleaned from tissue residues with a drop of $H_2O_2$ (3 %, AppliChem, Darmstadt, Germany). Using four reference points (bregma, lambda, and two points 2 mm to the left and to the right of the midline respectively), the animal's head was positioned into a skull-flat configuration for the further steps.

#### *Virus injection*

In order to suppress V1 L6 CT FB selectively and reversibly, we conditionally expressed the chloride-conducting channelrhodopsin stGtACR2 (*44, 80, 81*) in L6a CT pyramidal cells (*62, 57, 58*) by injecting AAV-stGtACR2-RFP into the left hemisphere V1 of Ntsr1-Cre mice (*45, 82, 83*) (**Figure 1a**). Ntsr1+ neurons are known to correspond with > 90% specificity to L6CT pyramidal cells (*11, 84, 85*). Furthermore, the opsin *stGtACR2* restricts expression to somata and the axon-initial segment which prevents possible accidental axonal depolarization due to a differential $Cl^-$ ion reversal potential across different neuronal compartments (*86, 87, 88*). It also offers improved photocurrents and higher sensitivity, which are of particular relevance to manipulating deeply located L6 CT neurons, while avoiding light artifacts and tissue damage arising from excessive light intensities (*88*).

Before surgery, the Cre-dependent, stGtACR2-expressing *adeno-associated virus* (AAV) vector (pAAV_hSyn1-SIO-stGtACR2-FusionRed, Addgene, #105677) stock solution was diluted to $5\times10^{11}$ gc/ml titers, and aliquotted to 4 $\mu$L.

During surgery, aliquots were front-loaded into a glass pipette mounted on a Hamilton syringe (SYR 10 $\mu$L 1701 RN no NDL, Hamilton, Bonaduz, Switzerland), controlled by the Injection Robot of the Neurostar Stereotax. After performing a small craniotomy for injection (100 $\mu$m diameter), we injected 300 nl of virus solution into V1 (2×50 nl shots injected at a rate of 50 nl / 30 s at a respective depth of 900 $\mu$m, 800 $\mu$m and 700 $\mu$m below the brain surface.

#### *Head-post and ground and reference screw implantation*

For implant fixation, the exposed skull was covered with OptiBond FL primer and adhesive (Kerr Dental, Rastatt, Germany) omitting three locations: V1 (AP: −3.28 mm, ML: −2.4 mm), dLGN (AP: −2.3 mm, ML: −2 mm), and a position roughly 1.5 mm anterior and 1 mm to the right of bregma, designated for a miniature ground and reference screw.

A custom-made lightweight stainless steel head bar was positioned over the posterior part of the skull such that the round opening in the bar was centered on V1/dLGN. The head bar was attached with dental cement (Ivoclar Vivadent, Ellwangen, Germany) to the primer/adhesive. The opening was later filled with the silicone elastomer sealant Kwik-Cast (WPI Germany, Berlin, Germany). Then the miniature screw (00-96 X 1/16 stainless steel screws, Bilaney), which served both as ground and reference that was soldered to a custom-made connector pin, was implanted.

#### *Post-surgical treatment and animal setup habituation*

At the end of the procedure, an iodine-based ointment (Braunodivon, 10%, B. Braun, Melsungen, Germany) was applied to the edges of the wound and a long-term analgesic (Meloxicam, 2 mg/kg, sc, Böhringer Ingelheim, Ingelheim, Germany) was administered and for 3 consecutive days. For at least 5 days post-surgery, the animal's health status was assessed via a score sheet.

After at least 1 week of recovery, animals were gradually habituated to the experimental setup by first handling them and then simulating the experimental procedure. To allow for virus expression, neural recordings started after an incubation time of 2-4 weeks after injection.

#### *Craniotomy*

On the day prior to the first day of recording, mice were fully anesthetized using the same procedures as described for the initial surgery, and a craniotomy (ca. 2×1 mm on the AP×BL axes) was performed over dLGN (ca. 2.5 mm posterior from bregma and 2.3 mm lateral from midline) and V1 and re-sealed with Kwik-Cast (WPI Germany, Berlin, Germany). As long as the animals did not show signs of discomfort, the long-term analgesic Metacam was administered only once at the end of surgery, to avoid any confounding effect on experimental results. Recordings were performed daily and continued for as long as the quality of the electrophysiological signals remained high.

### Extracellular multi-electrode array (MEA) recordings

After 2-4 weeks of incubation time, we performed *in vivo* extracellular multi-electrode array (MEA) recordings of dLGN neurons in awake, head-fixed mice (**Figure 1a**). Extracellular signals were recorded at 30 kHz (Blackrock microsystems, Blackrock Microsystems Europe GmbH, Hanover, Germany). For each recording session, the silicon plug sealing the craniotomy was removed. For dLGN recordings, a 32 channel linear silicon probe (Neuronexus A1x32Edge-5mm-20-177-A32) was lowered to a depth of ∼ 2700–3500 $\mu$m below the brain surface. We judged recording sites to be located in dLGN based on the characteristic progression of RFs from upper to lower visual field along the electrode shank (*50*), the presence of responses

strongly modulated at the temporal frequency of the drifting gratings (F1 response), and the preference of responses to high temporal frequencies (*54*, *50*). For *post hoc* histological reconstruction of the recording site, the electrode was stained with DiI (Invitrogen, Carlsbad, USA) for some (typically the last) recording sessions.

### Locomotion

During the experiment, mice were free to run on an air-floating Styrofoam ball and the run speed was recorded via locomotion sensors (**Figure 1a**). Two optical computer mice interfaced with a microcontroller (Arduino Duemilanove) sampled ball movements at 90 Hz.

To compute animal run speed, we used the Euclidean norm of three perpendicular components of ball velocity (roll, pitch and yaw) and smoothed traces with a Gaussian kernel ($\sigma$ = 0.2 s). To quantify the effect of running vs. sitting on various response properties, the run modulation index ($MI_{Run}$) was defined based on the mean firing rates during running vs. sitting periods as

$$MI_{Run} = \frac{\text{running} - \text{sitting}}{\text{running} + \text{sitting}}, \tag{1}$$

where running periods were defined as those for which speed exceeded 1 cm/s, and sit periods as those for which speed fell below 0.25 cm/s.

To test for a significant difference in mean FRs between the run vs. sit conditions matched for each neuron, we used the Wilcoxon signed-rank test (**Figure 1i**).

### Eye tracking

To record eye position and pupil size, the animal's eye that was viewing the stimulus was illuminated with infrared LED light and monitored using a zoom lens (Navitar Zoom 6000) coupled with a camera (Guppy AVT camera; frame rate 50 Hz, Allied Vision, Exton, USA).

Pupil position was extracted from the eye-tracking videos using a custom, semi-automated algorithm. Briefly, each video frame was equalized using an adaptive bi-histogram equalization procedure, and then smoothed using median and bilateral kernels. The center of the pupil was detected by taking the darkest point in a convolution of the kerneled image with a black square. Next, the peaks of the image gradient along lines extending radially from the center point were used to define the pupil contour. Lastly, an ellipse was fit to the contour, and the center and area of this ellipse was taken as the position and size of the pupil, respectively. A similar procedure was used to extract the position of the corneal reflection (CR) of the LED illumination. Eye-closure, grooming, or implausible ellipse fitting was automatically detected and the adjacent data points 0.15 s before and after were excluded. Linear interpolation and a subsequent Gaussian smoothing ($\sigma = 0.06$ s) was applied to fill the removed segments. Adjustable algorithm parameters, such as the threshold of the mean pixel-wise difference between each frame and a reference frame to detect blinks, were set manually for each experiment.

To quantify the effect of large vs. small pupil sizes on various response properties, the eye modulation index ($MI_{Eye}$) was defined based on the mean firing rates during periods of large vs. small pupils as

$$MI_{Eye} = \frac{\text{pupil large} - \text{pupil small}}{\text{pupil large} + \text{pupil small}}, \tag{2}$$

where periods of large pupils were defined as those for which pupil size was above the 50$^{\text{th}}$ percentile of the median normalized pupil trace, and periods of small pupils as those for which pupil size fell below the 25$^{\text{th}}$ percentile.

### Optogenetic feedback suppression

To photosuppress V1 Ntsr1+ L6CT pyramidal cells, an optic fiber (480 $\mu$m core diameter, MFP_480/500/1000-0.63_m_SMA, Doric Lenses, Quebec, Canada) was coupled to a light-emitting diode (blue LED, center wavelength 465 nm, LEDC2_465/635_SMA, Doric Lenses, Quebec, Canada) and positioned with a micromanipulator less than 1 mm above the exposed surface of V1. A black metal foil surrounding the tip of the head bar holder prevented the photostimulation light from reaching the animal's eyes. To ensure that the photostimulation was effective, the first recording session for each mouse was carried out in V1. Only if the exposure to light reliably induced suppression of V1 activity was the animal used for subsequent dLGN recordings. LED light intensity was adjusted on a daily basis to evoke reliable effects and account for variations in exact virus titer, volume, incubation time, virus expression levels, and fiber position (0.85-9.5 mW at the fiber tip). Since the tip of the fiber never directly touched the surface of the brain, and since the clarity of the surface of the brain varied (generally decreasing every day following the craniotomy), the light intensity delivered even to superficial layers of V1 was inevitably lower. For the movie stimulus, optogenetic pulses of 1 s duration were sent randomly each second with a 50 % chance.

To quantify the effect V1 L6CT suppression on various response properties, we defined the optogenetic modulation index ($MI_{Opto}$) based on the mean FRs during L6CT FB suppression ('opto') versus the control condition as

$$MI_{Opto} = \frac{\text{opto} - \text{control}}{\text{opto} + \text{control}} \tag{3}$$

## Visual stimulation

During the experiment, the mice were passively viewing visual stimuli on an LCD monitor screen in their right visual field. The visual stimuli were presented on a gamma-calibrated liquid crystal display (LCD) monitor (Samsung SyncMaster 2233RZ, 47×29 cm, 1680×1050 resolution at 60 Hz, mean luminance 50 cd/m$^2$) positioned at a distance of 25 cm from the animal's right eye (spanning $\sim$ 108×66° visual angle by small angle approximation) using custom written software (EXPO, https://sites.google.com/a/nyu.edu/expo/home). The display was gamma-corrected for the presentation of artificial stimuli, but not for movies (see below).

To quantify how much a neurons' firing rate is modulated by the visual stimulus, we defined the stimulus modulation index ($MI_{Stimulus}$) defined as

$$MI_{Stimulus} = (1 - MI_{Opto})(1 - MI_{Run})(1 - MI_{Eye}) \tag{4}$$

### *Movie stimulus*

For movie stimulus generation, we adopted a set of randomly picked clips from various movies. Briefly, source movie clips were converted to grey scale, temporally downsampled to 30 frames per s, spatially resampled and cropped to 424×264 pixels, to be presented on our 47×29 cm monitor screen at 25 cm distance at 106×66° (4 pixels/°) visual angle (by small angle approximation, which preserves the desired pixel resolution at the screen center better than the arctangent). Movie frames were not histogram-equalized and presented at 60 Hz (repeating each frame twice) without monitor gamma correction, since cameras are already gamma corrected for consumer displays (*89*). To generate the movie sequence, we used a random set of 296 unique movie clips (5 s each) and split 188/296 clips into 8 parts of 36 unique clips (5 s×36 = 180 s per part). They were interleaved with set of 8 clips (5 s×8 = 40 s) which was repeated 9 times. The repeated clips served to give an estimate of response reliability to the same clips. The movie sequence was flanked by a period of blank grey screen presentation (1 min) at the beginning and at the end, to record spontaneous activity. This resulted in a total stimulus duration of $\sim$ 32 mins. To rule out sequence effects, we randomized the clip order for different stimulus presentations. To investigate the effects of L6 CT FB suppression, we simultaneously presented a random optogenetic pulse train of 1 s pulses, occurring each second with a probability of 50 %, throughout the entire stimulus duration, including blank grey screen periods.

### *Sparse noise stimulus*

To measure receptive fields (RFs) in a more standard manner, we also presented an (artificial) sparse noise stimulus. The stimulus consisted of a rapid sequence of non-overlapping white and black squares appearing in succession within a 12x12 square grid presented on a grey background of mean luminance (50 cd/m$^2$). The square grid spanned 60° per side, while individual squares spanned 5° per side. Each square flashed for 200 ms.

## Histology

To verify virus expression and recording sites, we performed post-mortem histological analyses. After the final recording session, mice were first administered an analgesic (Metamizole, 200 mg/kg, sc, MSD Animal Health, Brussels, Belgium) and following a 30 min latency period were transcardially perfused under deep anesthesia using a cocktail of Medetomidin (Domitor, 0.5 mg/kg, Vetoquinol, Ismaning, Germany), Midazolam (Climasol, 5 mg/kg, Ratiopharm, Ulm, Germany) and Fentanyl (Fentadon, 0.05 mg/kg, Dechra Veterinary Products Deutschland, Aulendorf, Germany) (ip). Perfusion was first done with Ringer's lactate solution followed by 4% paraformaldehyde (PFA) in 0.2 M sodium phosphate buffer (PBS). Brains were removed, postfixed in PFA for 24 h, and then rinsed with and stored in PBS at 4° C. Slices (50 $\mu$m) were cut using a vibrotome (Leica VT1200 S, Leica, Wetzlar, Germany), stained with DAPI-solution (DAPI, Thermo Fisher Scientific, Waltham, Massachusetts, USA), mounted on glass slides with Vectashield mounting medium (Vectashield H-1000, Vector Laboratories, Burlingame, USA), and coverslipped. A scanning fluorescent microscope (BX61, Olympus, Tokyo, Japan) was used to inspect slices for the presence of red fluorescent protein (RFP/FusionRed) marking stGtACR2-channels, and DiI, marking electrode tracks. Recorded images were processed off-line using FIJI (*90, 91*).

## Spike sorting and unit extraction

Spike sorting was performed to obtain single unit activity from extracellular recordings. Electrophysiological signal recordings were kerneled using a 4$^{th}$-order Butterworth high-pass non-causal kernel with a low frequency cutoff of 300 Hz. We then used the open source, MATLAB-based (The Mathworks, Natick, Massachusetts, USA), automated spike sorting toolbox

Kilosort and Kilosort2 (*92*). Resulting clusters were manually refined using Spyke (*93*), a Python application that allows for the selection of channels and time ranges around clustered spikes for realignment, as well as representation in 3D space using dimension reduction (multichannel PCA, ICA, and/or spike time). In 3D, clusters were then further split via a gradient-ascent based clustering algorithm (GAC) (*94*). Exhaustive pairwise comparisons of similar clusters allowed the merger of potentially over-clustered units. For subsequent analyses, we inspected autocorrelograms and mean voltage traces, and only considered units that displayed a clear refractory period and a distinct spike waveshape.

### Data analysis

Data analysis was performed using custom-written code that applies general tools such as Numpy, sklearn, matplotlib, seaborn, pandas and carried out in a MySQL-based database using the DataJoint (*95*). We also used a customized version of RFEst (https://github.com/berenslab/RFEst) to allow for multiple model inputs.

### Firing rate calculations

To obtain units firing rates in spikes per second (Hz), each unit's spike density function (SDF) was calculated by binning spikes into a firing rate histogram (bin width = 20 ms) and convolving this with a Gaussian of width $2\sigma$ = 10 ms. Mean firing rates (FRs) over a given condition were calculated as the mean of the time-varying firing rates for the defined periods.

### Response reliability

To compute how reliable a neurons responded to the visual stimulus we used the set of 8 clips that where repeated 9 times throughout the experiment. We computed reliability by correlating each repetition with the mean of all other repetitions and averaging that over all splits.

### Exclusion criteria

Neurons with mean evoked firing rates $< 0.1$ Hz were excluded from all further analysis. Further analysis-specific selection criteria are stated in the appropriate subsections.

### Predictor correlations

To test for the correlations between the predictors *stimulus, opto, run, and eye*, we temporally aligned these traces, including only time points for which we had data points in all traces (e.g. removing periods of eye blinks). We then explored their cross-correlations in order to detect potential delays in their effects on each other. Such is the case, for instance in the pupil light reflex, where increases in stimulus intensity are followed by a delayed decrease in pupil size. We then used the delay time to shift the traces appropriately before computing their correlation value (Pearson's $r$; **Figure 1k**).

In order to test for statistical significance of the obtained correlation values , we first needed to account for the fact that our time-series inherently contain autocorrelations which would lead to an overestimation of correlations between them (except for the random opto pulses) (*51*). We therefore used a permutation test in which we randomly permuted the stimulus traces for $k = 1000$ iterations, and then computed the p-value of the observed correlation value as its percentile within the null distribution of p-values for the permuted traces (*51*).

### Spline-based generalized linear model

To estimate the spatio-temporal receptive fields (STRFs), we used the RFEst Python toolbox for spline-based spatio-temporal RF estimation (*43*). Here, the receptive field is parameterized with a set of basis functions. This reduces the number of hyperparameters compared to alternative approaches of receptive field estimation (such as automatic smoothness determination (*96*) or automatic locality determination (*97*)). RFEst is also less data demanding and reduces the computation time significantly (*43*). The number of parameters are given by the number of basis functions, also referred to the degrees of freedom. By using natural cubic splines as the basis the estimates are automatically smooth, which is a desirable property for single STRFs. To impose sparsity on the weights (also a desirable property of SRFs) we added L1 regularization, which pushed the weights for less relevant bases to zero. To compute the spline-based STRFs, $w_{SPL}$, the coefficients, $b_{SPL}$, were obtained as

$$b_{SPL} = (S^T X^T X S)^{-1} S^T X^T y \tag{5}$$

with $X$ as the stimulus design matrix, $y$ as the neural response vector, and $S$ as the spline matrix. The spatio-temporal RF was computed as

$$w_{SPL} = S b_{SPL} = S(S^T X^T X S)^{-1} S^T X^T y \tag{6}$$

To generate the natural cubic spline matrices ($S$) the package Patsy (0.5.1) is integrated into RFEst.

To approximate $w_{SPL}$ we used a generalized linear model (GLM) that predicts the instantaneous firing rate for one neuron using the movie as a predictor. We extended this "Stimulus only" model by integrating also running speed and pupil size as behavioral predictors of neuronal firing rate. To estimate the effect of cortico-thalamic (CT) feedback, an additional bimodal input was used comprising the optogenetic light stimulation that could be either on ($o_t = 1$) or off ($o_t = 0$). All inputs where parameterized with a set of spline basis and multiplied with an extra weight vector (also referred to as kernel):

$$f(s,o,r,e) = g(w_s^T\ s[t:t-\Delta t] + w_o^T o[t:t-\Delta t] + w_r^T r[t:t-\Delta t] + w_e^T e[t:t-\Delta t]) \tag{7}$$

with $s$, $o$, $r$, and $e$ denoting the additional model inputs of stimulus, optogenetics, running and eye, respectively, and $[t:t-\Delta t]$ defining the temporal integration window (250 ms for stimulus and 800 ms for non-retinal predictors).

We estimated the kernels by gradient descent with respect to the cost function with L1 regularization. The data set was divided into a training set (80 %, 150/188 unique movie clips) and a held out test set (final 20 %, 38/188 unique movie clips), which was untouched during hyperparameter selection. Using the final 20% of the data as test set is standard procedure for fitting models on time series data to preserve temporal relation during testing. To select optimal hyperparameters, we used five-fold cross-validation grid search on the training data (120 training clips and 30 validation clips in each fold). Hyperparameters included the number of spline basis (between 10 and 19) in temporal dimension (for stimulus, pupil size, locomotion, and feedback input) and spatial dimension (only stimulus), as well as the strength of the L1 regularization (with weights varying from 5 to 15). The STRFs were initialized randomly and optimized using gradient decent for 2000 iterations. We stopped the fitting early when the training cost changed less than $10^{-5}$ for 10 iterations. Finally, we selected the hyperparameters based on the mean performance on the validation set across folds. After optimal hyperparameter selection, models were retrained on the full training data (150 movie clips) and the final performance of the model was reported as the correlation coefficient between predicted and observed neural responses on the held out test data (38 movie clips).

### Session based permutation test

Following Harris (2020) (*51*), we performed a permutation test to evaluate if data from a different experimental session would lead to the same or worse model performance, which indicated the significance of the input-output correlations captured by the model. To achieve this, we provided the model with input data from the validation set of an unrelated session (for the model inputs ‘stimulus’, ‘running’, ‘pupil size’) or with synthetic inputs generated with the same statistics as the original (for the ‘CT feedback suppression’ input), one at a time. We repeated the process using all different data from all recording sessions. Subsequently, we compared for each input the actual model performance (Pearson’s $r$) on the validation set across its folds (n=5) against a distribution of model performances with that specific input permuted from the different recording sessions across their folds (n=5 folds $\times$ 9 recording sessions). Inputs were considered significant if the actual performance differed from the permuted performance with $p \leq 0.05$ using the non-paired Mann-Whitney-U test.

### Spatio-temporal RF component extraction

To separate spatial and temporal components of the 3D STRFs, we performed singular value decomposition (SVD) on the norm of the stimulus weight vector $w$. The temporal RF is extracted as the first left-singular vector of $U$, i.e. temporal dimension with the highest variance, and the spatial RF as the first right-singular vector of $V$, reshaped into the height- and width-dimensions of the input vector $w$. The extremes of the reshaped spatial RF vector are then used to quantify RF position and RF area. The extracted temporal RF components were normalized and multiplied with the RF center value before computing the slope (-150 ms to peak).

### Spatial RF contour estimation

Model spatial RFs were estimated by extracting the 2D spatial RF component from the model weights (see subsection ’Spatio-temporal RF component extraction’), and then drawing a contour line around the largest absolute peak (assumed to be the center of the spatial RF). The contour threshold gets gradually lowered until any further decrease would result in a second contour around the second largest extremum (background irregularities considered as noise). To avoid overly large RFs in very clean spatial components (without any major second extremum), the contour threshold had to be 2 standard deviations above or below the mean. To improve estimate accuracy, the spatial RF component was upsampled 16-fold via cubic spline interpolation.

### Spatial RF area

The spatial RF areas were estimated by using the spatial RF component and contour (see subsection ’Spatial RF contour estimation’) and calculating the number of pixels of the spatial RF contour mask in relation to the total number of pixels in the image frame, which was then scaled by the stimulus extent to obtain the value in squared degrees of visual angle. To improve estimate accuracy, the spatial RF component was upsampled 16-fold via cubic spline interpolation.

### Spatial RF center-surround

stRFs were collapsed across the azimuth axis, and accordingly defined as a function of elevation and time. Then, we identified the time point with peak activity. Subsequently, centre regions were defined according to the spatial width of the peak activity, and surround regions were defined as a ring encircling the centre and extending up to trice the diameter or 9°. We then summed pixel intensities within the centre region and the surround regions separately and calculated surround-to-centre ratio as:

$$surround-to-center = \frac{2 * \sum centre}{\sum surround_1 + \sum surround_2} \tag{8}$$

### Functional cell types clustering

To categorize neurons into functional subtypes, we employed dimensionality reduction (PCA) on their PSTH responses to a full-field light intensity step stimulus. Subsequently, we conducted clustering using a Gaussian mixture model on the principal components, resulting in the identification of four primary groups (Sustained ON, Sustained OFF, Transient, and Mixed). Nevertheless, we observed substantial response diversity even within these main groups. To address this, we further subdivided neurons within each group through empirical selection of cluster numbers, aiming to optimize silhouette scores and reduce the standard error of the PSTH mean response within the subclasses.

### Rate of change (RoC) to CT feedback suppression

To quantify the temporal dynamics of the effect of suppressing CT feedback with optogenetic pulses, we calculated rate of change (RoC) in the neurons' responses based on both data and model prediction. For each case, we first identified the time point $t_{min}$ where the slope of neurons response flipped its sign (e.g. after light onset, firing rates decreased, negative slope, and then it either stays constant or fluctuates around its new value and the slope becomes zero or flips its sign to positive). Then, we calculated the normalised change in responses $MI_{opto}$; (see subsection 'Optogenetic feedback suppression'). Finally, $RoC$ was defined as:

$$RoC = \frac{MI_{opto}}{t_{min}} \tag{9}$$

### Decoding analysis

We used a two-alternative forced choice (2AFC) decoder (*35*) to analyze if stimulus discriminability is easier with or without feedback. Given two spike trains $\{s_A, s_B\}$ in response to two movie clips $\{A, B\}$ we computed the model log-likelihood for the correct $((s_A, A), (s_B, B))$ and the incorrect pairing $((s_A, B), (s_B, A))$. We used the 'Full model' to predict spike trains in the two feedback conditions, (1) with the feedback component intact and (2) with the feedback component suppressed. In both conditions, we used 100 randomly selected 50 ms movie clips from the test set and their corresponding responses. Using all possible pairs, we computed the model log-likelihood for the correct and the incorrect pairing in both feedback conditions. The log probability for the correct pairing of response $s_A$ and stimulus $A$ is defined as follows:

$$\log p(s_A|A) = \sum_t s_{A,t} \log \lambda_t(A_t) - \lambda(A_t) \tag{10}$$

where $\lambda$ is the instantaneous firing rate at time $t$ predicted by the model. Analogously, we computed $\log p(s_B|B)$, $\log p(s_A|B)$, and $\log p(s_B|A)$. A correct choice was made if $\log p(s_A|A) > \log p(s_A|B)$ or $\log p(s_B|B) > \log p(s_B|A)$, respectively. We used the percentage correct over all possible pairs to quantify decoding performance. Finally, we computed the ratio of percentage correct for the feedback suppressed condition and the control condition. A ratio above one indicates better decoding performance in the feedback suppressed condition and a ratio below one in the control condition.